Int. J. Rock Mech. Min. Sci. & Geomech. Abstr. Vol. 29, No. 4, pp. 379–400, 1992
Printed in Great Britain.

0148-9062/92 $5.00 + 0.00

The Spectral Boundary Element Method: a New Window on Boundary Elements in Rock Mechanics

A. P. PEIRCE†
S. SPOTTISWOODE‡
J. A. L. NAPIER‡

This paper describes a novel spectral method based on the FFT for solving boundary integral equations incorporating the effect of non-linear material behaviour. The mathematical properties of this method are developed and illustrated by means of a simple model problem. The spectral boundary element technique is shown to provide a new framework for volumetric modelling with easy access to a number of interesting features not available to spatially implemented algorithms. A fundamental set of point Fourier kernels is introduced from which a variety of approximation schemes (including standard piecewise polynomial approximations) can be constructed in the frequency domain by introducing high frequency filters. The frequency domain implementation of these approximation schemes avoids the tedious integrations associated with spatial discretizations of the integral equations and provides considerable flexibility for general-purpose user-defined approximation schemes. Techniques are described to overcome the periodicity constraint imposed by the FFT so that general non-repeating geometries can be modelled. It is shown how the same periodicity can also be exploited to model repeating geometries. Two novel iterative methods are described to solve the discretized BE equations efficiently. The first method uses the information provided by the FFT to construct an approximate inverse extremely efficiently for use in a preconditioned conjugate gradient algorithm. This method can reduce the operation count for solution of the discretized problem to O(N log N) operations. The second method is an adaptation of Jacobi iteration which can roughly double the convergence rate for linear problems and can help to inhibit undesirable simultaneous failure of neighbouring elements when modelling brittle rock fracture. Two appendices containing expressions for the boundary element kernels and their Fourier transforms are provided.

INTRODUCTION

In the design of deep underground excavations there is a need to account for the inelastic deformation of the surrounding rockmass to give a more realistic estimate of the level of seismicity than the elastic calculations commonly used [1]. In addition, an understanding of the fracturing process around underground excavations will assist in the design of better support systems and help to explain (and possibly to control) the hard zones of rock that occur ahead of stope faces which inhibit the progress of the mining process.

The boundary element (BE) method [2] is the most efficient technique for modelling tabular excavations in 2- and 3-D elastic media with isolated slip planes. This is because the BE method effectively reduces the dimension of the discretization by one and because it automatically models infinite domains without requiring special treatment of the infinite boundary by mapped elements. However, the rock fracture in the vicinity of deep tabular excavations is often more intensive, pervasive and extensive than can practicably be modelled by traditional BE models with isolated slip planes. Therefore, a continuum volumetric damage approach such as is provided by the finite difference method [3], the finite element method or the extended BE method [4, 5] for modelling inelastic behaviour is more appropriate. Without modification the extended BE method loses many of its advantages

†Department of Mathematics and Statistics, McMaster University, Hamilton, Ontario, Canada.
‡Rock Engineering Division, COMRO, South Africa.

over the conventional domain discretization procedures such as the finite difference and finite element methods. In fact, the fully populated BE matrices serve to make the extended BE technique much less efficient than the domain methods. However, the special convolution structure of the BE matrices can be exploited using the fast Fourier transform (FFT) to make the BE technique a viable competitor to the other domain discretization techniques.

Rather than being merely an efficient way to perform convolution products, we have discovered that the FFT provides a whole new set of modelling options. Among other features the FFT approach allows: the conventional piecewise polynomial collocation approximations to be implemented almost trivially in a unified fashion by the implementation of the appropriate high-frequency filters; a great deal of flexibility in introducing new classes of approximations by means of filtering; self-replicating kernels to be generated automatically for the modelling of periodically repeated geometries; the efficient construction of spectral preconditioners for rapid solution of the algebraic equations that result from the discretization of the boundary integral equations; automatic access to frequency domain information about the solution such as the spectral distribution of plastic strain —which provides insight into the amount of small-scale (i.e. high-frequency) damage relative to the amount of large-scale (i.e. low-frequency) damage.

In the past 20 years the FFT has been extensively used to provide new approximate solution methods to partial differential equations known as spectral methods [6, 7]. The basic idea behind these spectral methods is the accurate representation of derivatives by multiplication operators in the frequency domain. Although we are also trying to solve partial differential equations, the class of numerical algorithms we propose is quite distinct from these spectral methods. For a linear elastic material we consider boundary integral representations of the solution in terms of special solutions. The technique we propose uses frequency domain representations of the special solutions and the FFT to arrive at new approximation schemes. In this paper we explore a number of features of this new "spectral boundary element formulation".

In the next section we introduce the classic boundary integral formulation for homogeneous elastic materials and the enhanced BE method for modelling inelastic material behaviour. In the third section we introduce the Fourier transform (FT), Fourier series and the discrete Fourier transform as well as some of their important properties. Since Fourier transforms are not widely used in rock mechanics, this section has been included to make the paper as self-contained as possible for the benefit of those readers unfamilar with the FT. In the fourth section, we briefly describe the piecewise polynomial collocation technique which is commonly used for the approximate solution of the boundary integral equations. In addition, we describe a model problem which is used throughout the paper to illustrate the spectral BE technique. We introduce the "point Fourier kernels", demonstrate some of their properties, and show how they can be used to construct approximation schemes in the frequency domain by introducing high-frequency filters. We demonstrate how the periodicity assumption of the FFT can be avoided if desired and how it can be exploited to model repeating geometries. In the fifth section, we discuss two iterative methods that can be used to solve the discretized BE equations efficiently. The first method uses the FFT to construct an approximate inverse extremely efficiently for use in a preconditioned conjugate gradient algorithm. The second method is an adaptation of Jacobi iteration which can roughly double the convergence rate for linear problems and inhibits undesirable simultaneous failure of neighbouring elements when modelling brittle rock fracture. In the last section, we summarize the findings of the paper. In Appendix A we derive a harmonic–biharmonic representation of the fundamental solutions required for the boundary integral equations. In Appendix B we provide the Fourier transforms of the fundamental solutions used to construct the discrete Fourier approximations.

THE BOUNDARY ELEMENT FORMULATION

Consider a region B in $\mathbf{R}^n$ bounded by ∂B and let $\bar{B}$ be that part of $\mathbf{R}^n$ exterior to B (see Fig. 1). Assume that B and $\bar{B}$ are occupied by homogeneous, isotropic elastic media. Let σ_{ij}, u_i and $\bar{\sigma}_{ij}$, $\bar{u}_i$ be the stresses and displacements in B and $\bar{B}$, respectively. The stresses in body B satisfy the equilibrium equations of elastostatics:

$$\sigma_{ij,j} + f_i = 0$$

and the stresses are related to the strains according to Hooke's law:

$$\sigma_{ij} = \frac{E}{2(1+\nu)}\left[\frac{2\nu}{1-2\nu}\delta_{ij}\epsilon_{kk} + 2\epsilon_{ij}\right],$$

where E is Young's modulus, ν is Poisson's ratio for the elastic medium and the definition of the strain tensor ϵ_{ij} in terms of the displacement field is:

$$\epsilon_{ij} = \tfrac{1}{2}(u_{i,j} + u_{j,i}).$$

The stress and displacement fields in $\bar{B}$ satisfy the same system of partial differential equations.

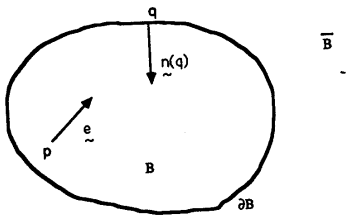

Fig. 1. Homogeneous, isotropic elastic media occupy the inner and outer regions B and $\bar{B}$ in $\mathbf{R}^n$ which are bounded by ∂B. The inward normal to the boundary ∂B at point q has components $n_i(q)$ and a point force with components $e_k(p)$ is applied at a point $p \in B$.

An application of Green's theorem to the above equations [5, 8] yields the following integral equations for u_k and σ_{kl}:

$$u_k(p) = \int_{\partial B} g(q_i, p_k) T_i(q) - G(q_{ij}, p_k) n_j(q) D_i(q)\, ds(q), \quad (1a)$$

$$\sigma_{kl}(p) = \int_{\partial B} \gamma(q_i, p_{kl}) T_i(q) - \Gamma(q_{ij}, p_{kl}) n_j(q) D_i(q)\, ds(q), \quad (1b)$$

where $T_i(q) = [\bar{\sigma}_{ij}(q) - \sigma_{ij}(q)] n_j(q)$ is the traction discontinuity and $D_i(q) = \bar{u}_i(q) - u_i(q)$ is the displacement discontinuity between the bodies $\bar{B}$ and B. The kernels are defined as follows: $g(q_i, p_k)$ is the kth displacement component at point p due to the ith traction discontinuity component at q; $G(q_{ij}, p_k) n_j(q)$ is the kth displacement component at point p due to the ith displacement discontinuity component at q; $\gamma(q_i, p_{kl})$ is the klth stress component at point p due to the ith traction discontinuity component at q; $\Gamma(q_{ij}, p_{kl}) n_j(q)$ is the klth stress component at point p due to the ith displacement discontinuity component at q.

Equations (1) are quite general in that all the direct and indirect BE formulations can be obtained from these equations. For example, if we remove the exterior body $\bar{B}$ and set the stresses and displacements $\bar{\sigma}_{ij} = \bar{u}_i = 0$ then (1a) reduces to the classical direct BE formulation. If we assume that the tractions (alternatively displacements) across ∂B are continuous then equations (1) reduce to the indirect BE formulation known as the displacement discontinuity (DD) method (alternatively the force discontinuity method). Because we are interested in representing the effect of geological discontinuities we shall pay particular attention to the DD formulation in the development of the FFT algorithms that follow. However, the techniques presented in this paper apply equally well to the other BE formulations. The kernels $g(q_i, p_k)$, $G(q_{ij}, p_k)$, $\gamma(q_i, p_{kl})$ and $\Gamma(q_{ij}, p_{kl})$ can be expressed in a succinct form in terms of derivatives of a biharmonic and a harmonic potential (see Appendix A).

The BE technique for a linear elastic medium can be extended [4, 5] to include inelastic material behaviour within the region B. This extension involves augmenting (1a) and (1b) by the following volume integrals representing the influence of the inelastic strain $\epsilon_{ij}^{(p)}$ throughout the body B:

$$(1a) + \int_B G(q_{ij}, p_k) \epsilon_{ij}^{(p)}(q)\, dv(q), \quad (2a)$$

$$(1b) + \int_B \Gamma(q_{ij}, p_{kl}) \epsilon_{ij}^{(p)}(q)\, dv(q). \quad (2b)$$

One of the primary advantages of the classical BE technique for elastic problems over domain discretization methods (such as finite differences and finite elements) is that equations (1) involve only unknowns on the boundary ∂B. This effectively reduces the problem from an n-dimensional problem to one in which unknowns are being sought in $n-1$ dimensions. The discretized BE equations (1) have small, fully populated matrices whereas the corresponding domain discretization methods involve large, sparse matrices. This makes the BE technique extremely competitive particularly for problems with small surface-to-volume ratios, which are typically found in geomechanics. However, when the effect of inelastic deformation is included, the BE technique would seem to lose much of its computational advantage particularly for problems involving extensive regions of inelastic deformation.

However, the integral equations (2) are convolution equations since their kernels are translation invariant in that their functional form depends only on the distance $|p-q|$ between the sending and receiving points. Discretization of (2) results in matrix equations that are fully populated but which inherit the convolution structure of the integral equations. For problems with significant amounts of inelastic strain $\epsilon_{ij}^{(p)}$ storage of the fully-populated influence matrices would be prohibitive. Direct elimination methods are, therefore, not suitable for solving these equations whereas iterative methods allow the convolution structure of the matrices to be exploited. The major computational burden in the iterative solution of these equations arises from the matrix–vector products associated with the volume integrals in (2), which are referred to as convolution products. If there are N volume elements then $O(N^2)$ operations are required to evaluate these products directly. There are two distinct ways of accelerating this process. The first technique, referred to as "lumping", exploits the rapid decay of the kernels G and Γ with distance $r = [(q_i - p_i)(q_i - p_i)]^{1/2}$ to calculate far-field influences by averaging the strain field $\epsilon_{ij}^{(p)}$ over a number of volume elements [5, 9]. Depending on the lumping scheme used it is possible to reduce the convolution computation from $O(N^2)$ to $O(N)$ operations. The second procedure uses the fast Fourier transform (FFT) to evaluate the convolution integrals in (2) [10]. Effectively the FFT diagonalizes the kernel matrices G and Γ so that the convolution products can be performed in N operations. Since the FFT for an N vector involves $N \log N$ operations the total asymptotic operation count is $O(N \log N)$.

The FFT was first exploited in this context by Stewart [11] to perform the convolution integrals in (1b) for DDs on a planar surface in three dimensions. In this paper we discuss the use of the FFT for evaluating the convolution products that result from discretizing planar surface integrals and the volume integrals in (2). We also use the FFT to obtain a new class of numerical approximations to the integral equations (2), which use kernels calculated from analytic Fourier transforms of G and Γ. This new class of kernels, which we refer to as the "point Fourier kernels", are quite fundamental in that all the standard piecewise polynomial approximations to (2) can be obtained as special cases as well as a number of new approximation schemes.

THE FOURIER TRANSFORM

In this section we introduce the basic definitions and properties of the Fourier transforms we will use in this paper. As Fourier transforms are not widely applied in rock mechanics we will also attempt to demonstrate how Fourier transforms provide a new perspective on the physical world.

The hierarchy of Fourier transforms

The Fourier transform on an infinite interval. Let $g \in L^1(-\infty, \infty)$ then we define the Fourier transform of g to be:

$$\mathscr{F}\{g\} = \hat{g}(f) = \int_{-\infty}^{\infty} \exp(-2\pi i f x) g(x)\, dx \quad (3a)$$

and the corresponding inversion formula is:

$$\mathscr{F}^{-1}\{\hat{g}\} = g(x) = \int_{-\infty}^{\infty} \exp(2\pi i f x) \hat{g}(f)\, df. \quad (3b)$$

Thus $\hat{g}(f)$ represents the Fourier amplitude of the function g at the frequency f. It is also common to define the FT in terms of the angular frequency $\omega = 2\pi f$ and we shall use the two frequencies interchangeably in the remainder of this paper. We refer to g and $\hat{g}$ as a transform pair one of which is sufficient to determine the other. Thus a function g can either be defined in physical space by prescribing all its values $g(x)$ or, equivalently, it can be defined by giving all its Fourier amplitudes $\hat{g}(f)$ in frequency (or wave number) space. We note that other than the integrability condition on g there are no other restrictions on g. Similarly for a function $g(x, y, z)$ of three variables the 3-D Fourier transform is defined to be:

$$\begin{aligned}\hat{g}(f_1, f_2, f_3) = &\int_{-\infty}^{\infty}\int_{-\infty}^{\infty}\int_{-\infty}^{\infty} \\ &\times \exp[-2\pi i(f_1 x + f_2 y + f_3 z)] \\ &\times g(x, y, z)\, dx\, dy\, dz \\ = &\int_{R^3} \exp[-2\pi i(\mathbf{f}\cdot\mathbf{r})] g(\mathbf{r})\, d\mathbf{r}^3 \end{aligned} \quad (3c)$$

and its corresponding inversion formula is:

$$g(\mathbf{r}) = \int_{R^3} \exp[-2\pi i(\mathbf{f}\cdot\mathbf{r})] \hat{g}(\mathbf{f})\, d\mathbf{f}^3.$$

Some useful properties of Fourier transforms:

Property (FT P1) implies that differentiation can be performed in the transformed space by the algebraic process of multiplication by $i(2\pi f)$. Parseval's relation (FT P3) provides insight into the distribution of strain energy in the spatial and wavenumber domains. The linearity property (FT P4) of the governing partial differential equations for an elastic body is exploited to derive the fundamental kernels in (1) and (2). The asymptotic behaviour (FT P7) provides useful insight into the relation between the smoothness of a function and the rate at which its high frequency Fourier amplitudes decay. Property (FT P8) enables spatial averages of a function to be established directly from its FT.

Fourier series. If we approximate the integral in the definition (3a) of the FT by a Riemann sum then we have:

$$\begin{aligned}&\int_{-\infty}^{\infty} \exp(-2\pi i f x) g(x)\, dx \\ &\qquad \approx \Delta \sum_{k=-\infty}^{\infty} g(x_k) \exp(-2\pi i f x_k) = \bar{g}(f). \end{aligned} \quad (4a)$$

Here Δ is the sampling width and $x_k = k\Delta$. The inverse transform corresponding to $\bar{g}(f)$ is:

$$g(x_k) = \int_{-1/2\Delta}^{1/2\Delta} \bar{g}(f) \exp(2\pi i f x_k)\, df. \quad (4b)$$

Thus the Fourier series (4) is an approximation to the Fourier transform (3) in which the function g is sampled at an infinite number of discrete points while the Fourier amplitude $\hat{g}(f)$ is sampled throughout the finite band of frequencies $[-1/2\Delta, 1/2\Delta]$. Alternatively, we note that the symmetric pair of Fourier transforms (3) could equally well have been approximated by sampling the function $g(x)$ over a finite interval while $\hat{g}(f)$ is sampled at an infinite number of discrete frequencies. In this case the Fourier series representation is of the form:

$$\bar{g}_k = \int_{-1/2}^{1/2} g(x) \exp(-2\pi i k x)\, dx \quad (4c)$$

and

$$g(x) = \sum_{k=-\infty}^{\infty} \bar{g}_k \exp(2\pi i k x). \quad (4d)$$

We note that the representation (4d) is periodic. If g is not a periodic function then (4d) will give a faithful representation of g on the sample interval $(-\frac{1}{2}, \frac{1}{2})$ but it will ignore the actual values of g outside this interval

---

(FT P1) Transform of a derivative: $g'(x) = i(2\pi f)\hat{g}(f)$
(FT P2) Transform of a convolution: $\mathscr{F}\{\int_{-\infty}^{\infty} g(x-y)h(y)\, dy\} = \hat{g}(f)\hat{h}(f)$
(FT P3) Parseval's relation: $\int_{-\infty}^{\infty} g^2(x)\, dx = \int_{-\infty}^{\infty} |\hat{g}(f)|^2\, df$
(FT P4) Linearity: $\widehat{\alpha g + \beta h} = \alpha\hat{g} + \beta\hat{h}$
(FT P5) If g is even [i.e. $g(-x) = g(x)$] then: $\hat{g}(f) = 2\int_0^{\infty} \cos(2\pi f x) g(x)\, dx$
(FT P6) $\hat{\hat{g}}(x) = g(-x)$
(FT P7) Asymptotic behaviour of FT: if $d^k g/dx^k(x) \in L^1$ then $\hat{g}(f) = o(1/f^k)$ as $f \to \infty$
(FT P8) Average value: $\hat{g}(0) = \int_{-\infty}^{\infty} g(x)\, dx$.

and only give periodic continuations of the values of g on the interval $(-1/2, 1/2)$.

The sampling theorem. A function whose frequency components are zero above a certain frequency [i.e. $\hat{g}(f)=0$ for $|f|>f_c$] is called a "band limited function". An important feature of a band limited function g is that it can be expressed in the following form:

$$g(x)=\Delta\sum_{n=-\infty}^{\infty} g(x_n)\frac{\sin[2\pi f_c(x-x_n)]}{\pi(x-x_n)}. \tag{5}$$

This representation implies that all the values $g(x)$ of the function g are completely determined by the discrete samples $g(x_j)$ taken at an interval $\Delta=1/2f_c$. Thus for a band-limited function, sampling the function more frequently than the spacing Δ will only give redundant information. In the numerical schemes based on the discrete FT we will be making the assumption that the approximate solutions are band limited. In this case representation (5) provides a means of interpolating between the known nodal values $g(x_n)$ to obtain the function values $g(x)$.

Analogous operational properties can be derived for the Fourier series as those given above for the Fourier transform in (FT P1–FT P8).

The discrete Fourier transform. The Fourier series is still not suitable for numerical modelling as function values are required at an infinite number of discrete points in (4a) or equivalently at the continuum of frequencies in (4b). We therefore introduce a further approximation by sampling $g(x)$ at only a finite number of points N on the interval $[-\frac{1}{2},\frac{1}{2}]$. Consider the N mesh points $x_j=j/N=j\Delta$; $j=-N/2,\ldots,N/2$, and the following approximation to the Fourier transform of $g(x)$:

$$\hat{g}(f_n)=\int_{-\infty}^{\infty}\exp(-2\pi i f_n x)g(x)\,dx$$

$$\approx\Delta\sum_{j=-N/2}^{N/2-1} g(x_j)\exp(-2\pi i f_n x_j). \tag{6}$$

If we assume that g is periodic [i.e. $g(x_{-N/2})=g(x_{N/2})$] then (6) represents a trapezoidal approximation to the Fourier transform $\hat{g}(f_n)$. Motivated by this approximation we define the discrete Fourier transform: assuming $f_n=n/N\Delta$:

$$\tilde{g}_n=\frac{1}{N}\sum_{j=0}^{N-1} g(x_j)\exp(-2\pi i n j/N). \tag{7a}$$

The corresponding inverse transform of (7a) can be determined by using the identity:

$$\frac{1}{N}\sum_{j=0}^{N-1}\exp(2\pi i q j/N)=\begin{cases}0, & q\neq nN,\\ 1, & q=nN,\end{cases} \tag{7b}$$

to obtain:

$$g(x_j)=\sum_{n=-N/2}^{N/2-1}\tilde{g}_n\exp(2\pi i n j/N). \tag{7c}$$

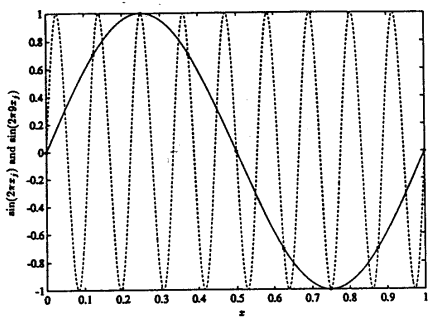

Fig. 2. The two modes $\sin(2\pi x_j)$ and $\sin(2\pi 9x_j)$. When sampled at the mesh points $\{x_j=j\Delta; j=0,\ldots,N=8; \Delta=1/N\}$, which are marked with asterisks, the two modes are indistinguishable.

We note that the discrete spatial sampling of g in (7a) results in an inverse representation (7c) in terms of a finite band of discrete frequencies. We also note that (7a) is often known as the discrete Fourier transform whereas the FFT refers to an efficient algorithm to calculate (7a) or its inverse (7c) (see e.g. [10]). However, since the FFT is always used to calculate (7a and c) we shall simply refer to (7a and c) as FFTs to avoid confusion.

Aliasing. In practice $g(x)$ is not band limited and we approximate g by a band-limited function. In this case the error made by assuming that the function is band limited can be seen by substituting (4d) into (7a) and using the identity (7b) to yield:

$$\tilde{g}_n=\bar{g}_n+\sum_{\substack{k=-\infty\\ k\neq 0}}^{\infty}\bar{g}_{n+Nk}. \tag{8}$$

Thus the FFT amplitude of the nth mode is equal to the nth Fourier coefficient plus the amplitudes of all those Fourier modes that "*alias*" the nth mode on the discrete mesh. Any mode that has the same values throughout the mesh x_j as the nth mode is said to alias the nth mode, because it is indistinguishable *on the mesh* from the nth mode. For an aliased mode m: $\exp[2\pi i(n/N\Delta)x_j]=\exp[2\pi i(m/N\Delta)x_j]\Leftrightarrow m=n+kN$ for $k\neq 0$, which are just the modes that form the sum in (8). In Fig. 2 we plot the two modes $\sin(2\pi x_j)$ and $\sin(2\pi 9x_j)$ and mark with asterisks the values of these two functions for those abscissae on the mesh: $N=8$ and $\Delta=1/N$. We observe that when sampled at the mesh point x_j these two modes are indistinguishable.

Some useful properties of the discrete Fourier transform:

(FFT P1) Periodicity:

$$\tilde{g}_{k+pN}=\tilde{g}_k;\qquad p=0,\pm1,\ldots;$$

$$g(x_{k+pN})=g(x_k);\quad p=0,\pm1,\ldots$$

(FFT P2) Transform of a convolution:

$$\mathrm{FFT}\{(a * b)_n\}_k = \mathrm{FFT}\{\Sigma_{m=0}^{N-1} a_{n-m} b_m\} = \tilde{a}_k \tilde{b}_k,$$

(FFT P3) Parseval's relation:

$$\Sigma_{j=0}^{N-1} |g(x_j)|^2 = \Sigma_{j=0}^{N-1} |\tilde{g}_j|^2.$$

Property (FFT P1) demonstrates the periodicity imposed by the FFT representation and its inverse. Property (FFT P2) is fundamental to this paper as it allows the costly process of convolution of two sequences [taking $O(N^2)$ operations if calculated directly] to be performed by calculating the product of the FFTs of the two sequences at each frequency [reducing the cost to $O(N \log N)$ operations].

Some useful transform pairs

In this section we give the Fourier transforms of some simple functions to illustrate some of the properties of the Fourier transform and provide information that will be used in the fourth section.

The Dirac delta function. The FT of the delta function $\delta(x)$ is given by:

$$\hat{\delta} = \int_{-\infty}^{\infty} \exp(-i\omega x)\, \delta(x)\, \mathrm{d}x = 1 \tag{9}$$

or

$$\hat{1} = \delta(\omega)$$

where

$$\omega = 2\pi f.$$

Thus the FT of the spike is a constant function in the wavenumber domain.

The rectangular box. The box function $b(x, \Delta)$ defined by:

$$b(x, \Delta) = \begin{cases} 0, & |x| > \Delta/2, \\ 1, & |x| \leqslant \Delta/2, \end{cases} \tag{10a}$$

has the following FT:

$$\hat{b}(\omega, \Delta) = \Delta \frac{\sin\left(\frac{\omega\Delta}{2}\right)}{\left(\frac{\omega\Delta}{2}\right)}, \tag{10b}$$

$b(x, \Delta)$ and $\hat{b}(\omega\ , \Delta)$ are plotted in Fig. 3a.

The Gibbs phenomenon. Numerical models based on the FT sometimes exhibit oscillations in the stress field known as the Gibbs phenomenon. The FT of the box function can be used to illustrate and explain this effect. The Gibbs phenomenon occurs when we try to approximate a discontinuous function such as $b(x, \Delta)$ [whose Fourier transform decays fairly slowly according to (FT P7)] by a band-limited Fourier expansion. Substituting $\hat{b}(\omega, \Delta)$ from (10b) into (3b) we obtain the representation:

$$b(x, \Delta) = \int_{-\infty}^{\infty} \exp(2\pi i f_x) \frac{\sin(2\pi f\, \Delta/2)}{(2\pi f)/2} \mathrm{d}f$$

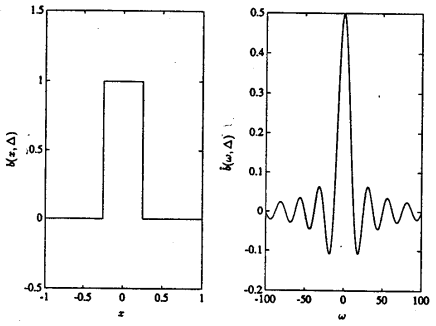

Fig. 3a. The box function $b(x, \Delta)$ and its Fourier transform $\hat{b}(\omega, \Delta)$.

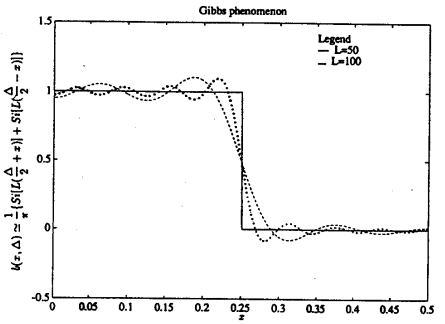

Fig. 3b. The function $b(x, \Delta)$ and the band-limited approximation (12) for $L = 50$ (– – –) and $L = 100$ ($\cdots$). Observe that the approximation (12) overshoots $b(x, \Delta)$ by a maximum of about 9% and which is located at the points $x = \pm\Delta/2 \mp \pi/L$. If we increase L we only make the positions of the peaks of successive approximations closer to the points $x = \pm\Delta/2$ but the amount of overshoot is the same for all $L < \infty$.

$$= \frac{1}{\pi} \int_0^{\infty} \frac{\sin \omega(\Delta/2 + x) + \sin \omega(\Delta/2 - x)}{\omega} \mathrm{d}\omega$$

$$= \begin{cases} 0, & |x| > \Delta/2, \\ 1, & |x| < \Delta/2, \\ \frac{1}{2}, & |x| = \Delta/2. \end{cases} \tag{11}$$

If instead of evaluating the above integral we truncate it after a finite length L then:

$$b(x, \Delta) \simeq \frac{1}{\pi} \left\{ Si\left[L\left(\frac{\Delta}{2} + x\right)\right] + Si\left[L\left(\frac{\Delta}{2} - x\right)\right]\right\}, \tag{12}$$

where $Si(x) = \int_0^x (\sin s/s)\, \mathrm{d}s$.

From Fig. 3b we observe that the band-limited approximation overshoots the function $b(x, \Delta)$ by a maximum of 9%. Since $Si(\pi) \simeq \frac{1}{2} + 1/\pi^2(1 - 2!/\pi^2 + \cdots)$ is the maximum of $Si(x)$ on $(0, \infty)$, we observe that the location of the maximum overshoot is at $x = \pm\Delta/2 \mp \pi/L$. Thus if we increase L we only make the positions of the peaks of successive approximations of the form (12) closer to the points $x = \pm\Delta/2$ but the amount of overshoot is the same for all $L < \infty$. It is only in the limit $L \to \infty$ that the correct Fourier representation (11) is

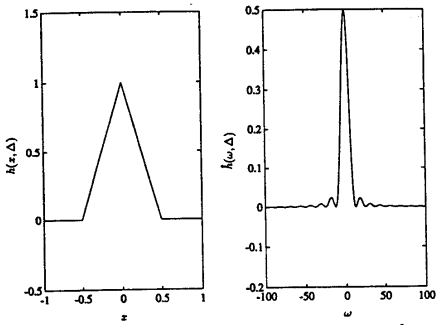

Fig. 3c. The hat function $h(x, \Delta)$ and its Fourier transform $\hat{h}(\omega, \delta)$.

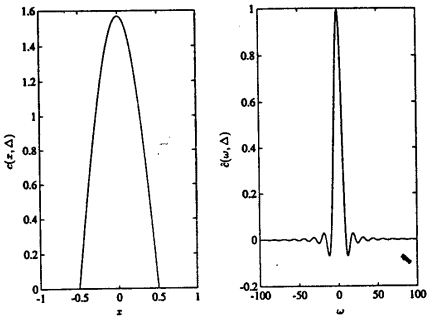

Fig. 3e. The cosine hat function $c(x, \Delta)$ and its Fourier transform $\hat{c}(\omega, \Delta)$.

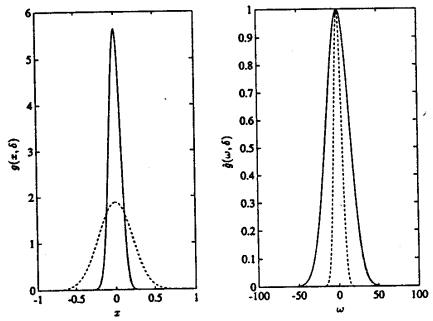

Fig. 3d. The Gaussian function $g(x, \delta)$ and its Fourier transform $\hat{g}(\omega, \delta)$ for two distinct values of δ: $\delta = 0.1$—solid line and $\delta = 0.3$—dashed line. Notice that decreasing δ makes g narrower and has the effect of making the FT of the Gaussian $\hat{g}$ more spread out since it contains more high-frequency components.

achieved. The Gibbs phenomenon is due to the slow rate of decay of the Fourier amplitudes

$$\hat{b}(\omega, \Delta) \overset{\omega \to \infty}{=} O(1/\omega)$$

which causes appreciable errors when the Fourier expansion is truncated. The remedy to the Gibbs phenomenon is to introduce filters to remove the high frequencies. We shall exploit filters in this paper and demonstrate how they can be used to introduce various approximation schemes.

The triangular hat. The triangular hat function $h(x, \Delta)$ defined by:

$$h(x, \Delta) = \begin{cases} 0, & |x| > \Delta \\ 1 - \dfrac{|x|}{\Delta}, & |x| \leqslant \Delta. \end{cases} \tag{13a}$$

has the following FT:

$$\hat{h}(\omega, \Delta) = \Delta \frac{\sin^2\left(\dfrac{\omega\Delta}{2}\right)}{\left(\dfrac{\omega\Delta}{2}\right)^2}, \tag{13b}$$

$h(x, \Delta)$ and $\hat{h}(\omega, \Delta)$ are plotted in Fig. 3c.

We notice that $h(x, \Delta)$ can be generated by convolving $b(x, \Delta)$ with itself so that:

$$h(x, \Delta) = (b * b)\left(x - \frac{\Delta}{2}\right)\Big/\Delta.$$

This relationship in the frequency domain can be expressed in the form:

$$\hat{h}(\omega, \Delta) = \hat{b}(\omega, \Delta)^2/\Delta,$$

which can be verified directly using (10b) and (13b). The way in which convolution with $b(x, \Delta)$ is a smoothing process becomes transparent when viewed in the frequency domain. In particular, multiplication by

$$\hat{b}(\omega, \Delta) \overset{\omega \to \infty}{=} O(1/\omega)$$

implies that the high frequencies of the resulting function decay by a factor $1/\omega$ faster so that according to (FT P7) the resulting function will have one more derivative. This smoothing process can be repeated to obtain functions with continuous derivatives. In fact by taking successive convolutions of the rectangular box with itself we can obtain qth order splines: $\Delta(\sin^{q+1}(\omega\Delta/2)/(\omega\Delta/2)^{q+1})$ (see for example Ref. [12]).

This example illustrates that convolution is a smoothing process since the convolution of two discontinuous functions, $b(x, \Delta)$ in this case, resulted in a continuous function $h(x, \Delta)$. We also notice that the Fourier coefficients of the continuous function $h(x, \Delta)$ decay more rapidly $O(1/\omega^2)$ than those of the discontinuous function $b(x, \Delta)$ as the frequency $\omega \to \infty$. We shall exploit the smoothing effect of convolution later when we introduce filters to smooth the high frequency Fourier components of the singular kernels of the integral equations (1) and (2).

Gaussians. The Gaussian function $g(x, \delta)$ defined by:

$$g(x, \delta) = \frac{\exp\left[-\left(\dfrac{x}{\delta}\right)^2\right]}{\sqrt{\pi\delta}}, \tag{14a}$$

has the following FT:

$$\hat{g}(\omega, \delta) = \exp\left[-\left(\frac{\omega\delta}{2}\right)^2\right]. \tag{14b}$$

Here the parameter δ, which is distinct from the mesh parameter Δ, is used to adjust the width of the Gaussian function. $g(x, \delta)$ and $\hat{g}(\omega, \delta)$ are plotted in Fig. 3d. We observe that $\hat{g}$ is also a Gaussian, and that if we decrease δ which makes g narrower then its FT $\hat{g}$ becomes more spread out (i.e. it contains more high-frequency components). In fact, since $g(x, \delta)$ is a delta sequence function, i.e.

$$g(x, \delta) \overset{\delta \to 0}{=} \delta(x)$$

we see from (14) that

$$\hat{g}(\omega, \delta) \overset{\delta \to 0}{=} 1,$$

which is another way of deriving (9).

The cosine hat. The cosine hat function $c(x, \Delta)$ defined by:

$$c(x, \Delta) = \begin{cases} 0, & |x| > \Delta, \\ \dfrac{\pi}{4\Delta} \cos\left(\dfrac{\pi x}{2\Delta}\right), & |x| \leqslant \Delta, \end{cases} \tag{15a}$$

has the following FT:

$$\hat{c}(\omega, \Delta) = \frac{\cos(\omega \Delta)}{1 - \left(\dfrac{2\omega\Delta}{\pi}\right)^2}. \tag{15b}$$

Both $c(x, \Delta)$ and $\hat{c}(\omega, \Delta)$ are plotted in Fig. 3e.

DISCRETIZATION AND THE POINT FOURIER KERNELS

In this section we describe the procedure commonly used to discretize the integral equations (2). We also introduce the notion of the "the point Fourier kernels" which are essentially frequency domain representations of the point force discontinuity and displacement discontinuity kernels in (1) and (2). We will demonstrate that the point Fourier kernels form a fundamental set of kernels from which a variety of approximation schemes (e.g. expansion of the solution in terms of piecewise constant or piecewise linear basis functions) can be obtained by the application of the appropriate filters in the frequency domain.

Discretization

The procedure commonly used to discretize the integral equations (2) is to divide the boundary ∂B into line segments and the region B into triangular or rectangular elements. The unknown fields T_i or D_i and $\epsilon_{ij}^{(p)}$ are then assumed to be constant, to vary linearly or quadratically over each of these elements. For example in the discretization of a 2-D problem, the contribution of the inelastic strain integral in (2b) can be expressed in the following form:

$$\sigma_{qr}^{ij} = \sum_{k,l} \Gamma_{qrst}^{i-k,j-l} \epsilon_{st}^{(p),kl}. \tag{16}$$

Here the subscripts have been used to denote the respective stress and strain components and the superscripts are used for the node numbers of the collocation points. The integrated kernels $\Gamma_{qrst}^{i-k,j-l}$ are usually evaluated analytically (see for example Ref. [5]).

The model problem

As another illustration of the typical discretization process used in the collocation method for solving the integral equations (1) and (2) we consider the special case of (1b) which represents a model of a crack located along the line $y = 0$ in a 2-D elastic body subjected to the normal stress distribution $p(x)$. In this case the DD distribution $U(\xi)$ is governed by [2]:

$$\frac{E}{4\pi(1-\nu^2)} \int_{-l}^{l} \frac{U(\xi)}{(x-\xi)^2} \mathrm{d}\xi + p(x) = \sigma[x, U(x)]. \tag{17a}$$

Equation (17a) expresses the fact that the superposition of the mining-induced stresses, represented by the integral in (17a), and the pre-existing stresses $p(x)$ should balance the load $\sigma[x, U(x)]$ carried by material within the crack when it has been compressed by an amount $U(x)$. In the absence of material within the crack (17a) expresses the condition that superposition of the mining-induced stresses and the pre-existing stresses should leave the boundary of the excavation stress free. In this paper (17a) will be used as a model problem to demonstrate the properties of a number of FFT algorithms. This model problem serves as a test for the performance of FFT-based discretizations of the classic DD integral equations (1b) as well as the DD integral equations (2b) which have been extended to model non-linear material behaviour.

As described above we discretize (17a) by dividing the interval $[-l, l]$ into N equal subintervals or elements of length Δ and assuming that over each of these subintervals $U(\xi)$ has some polynomial variation. The equations for the N unknown DD values associated with the piecewise constant approximation to $U(\xi)$ obtained by collocation at the midpoints $x_m = -l + (m - \frac{1}{2})\Delta$, $m = 1, \ldots, N$ of the elements are:

$$\sum_{m=1}^{N} A_{nm} u_m + p_n = \sigma(x_n, u_n), \tag{17b}$$

where

$$A_{nm} = \frac{\gamma}{\pi\Delta[(n-m)^2 - \frac{1}{4}]}; \quad \gamma = \frac{E}{4(1-\nu^2)}$$

and u_m is used to denote the numerical approximation to $U(x_m)$.

As an example we consider the special case when $p(x) = p =$ constant and $\sigma(x_n, u_n) = 0$ in which case the analytic solution to (17a) and its FT are:

$$U(x) = \frac{p}{\gamma}\sqrt{l^2 - x^2}; \quad \hat{U}(\omega) = \frac{2\pi l p J_1(l\omega)}{\gamma\omega}, \tag{17c}$$

where J_1 is the first-order Bessel function. Both this analytic solution and the solution to the discretized equations (17b) are plotted in Fig. 4a in the case $N = 16$.

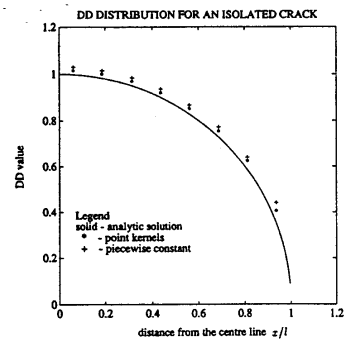

Fig. 4a. The analytic solution (17c) to (17a) in the case $p(x) = \gamma$ and the piecewise constant $u_{PWC,n}$ [see (17b)] and the point Fourier $u_{PT,n}$ approximate solutions for $N = 16$. The point Fourier DD distribution is more accurate than that of the piecewise constant approximate.

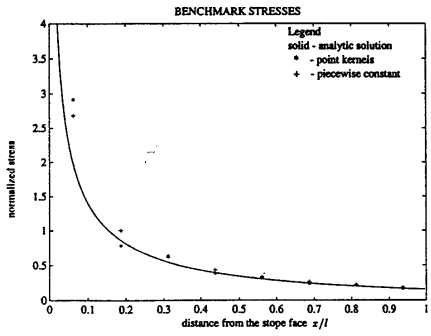

Fig. 4b. The analytic normalized stress distribution (17d) ahead of the crack-like excavation and the corresponding piecewise constant and point Fourier approximates. Because we are using a finite number of modes to represent a discontinuous function the point Fourier stresses exhibit Gibbs oscillations about the analytic values.

By using the approximate solution u_m the stress distribution along $y = 0$ can be obtained by evaluating the left-side of (17b) at the desired values of x. The piecewise constant approximate normalized stress distribution and the analytic normalized stress distribution:

$$\sigma(x) = \begin{cases} -1, & |x| < l, \\ \dfrac{x}{\sqrt{x^2 - l^2}} - 1, & |x| > l, \end{cases} \tag{17d}$$

are plotted in Fig. 4b for $x > l$. Away from the crack the approximate normalized stress distribution closely resembles that of the analytic solution.

Iteration using the FFT

For problems with significant amounts of inelastic strain $\epsilon_{ij}^{(p)}$ storage of the fully populated influence matrices would be prohibitive. Direct elimination methods are, therefore, not suitable for solving these equations whereas iterative methods allow the convolution structure of the matrices to be exploited to save storage and to reduce solution times. The iterative procedure used to solve (16) and (17b) is outlined in Fig. 5. We notice that (16) and (17b) both involve convolution products which form one of the most costly parts of this solution process. Indeed, if the discretization involves N nodes then $O(N^2)$ operations will be required to evaluate these

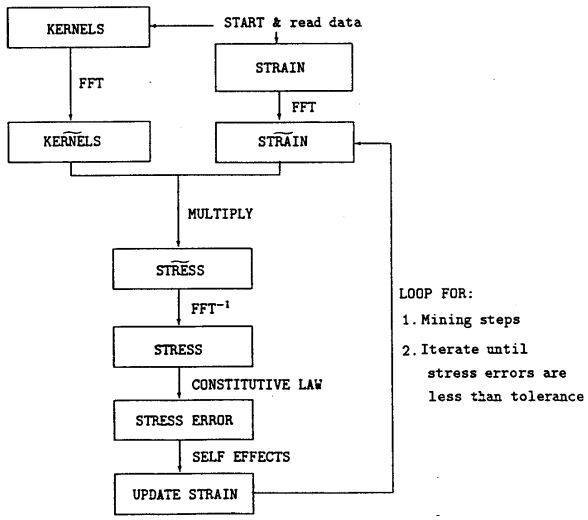

Fig. 5. A flowchart of an iterative procedure that uses the FFT to evaluate the convolution products by multiplication in the frequency domain. By performing these convolutions in the frequency domain the cost of calculating the trial stresses can be reduced from $O(N^2)$ to $O(N \log N)$ operations.

convolutions directly. If the discretization is on a uniform rectangular mesh [as is the case in (17b)] then the FFT can be used to effectively diagonalize the kernel matrices $\Gamma^{i-k,j-l}_{qrst}$ and A_{mn}. In this case, the convolution products in (16) and (17b) can be evaluated by multiplying the FTs of the kernels by the FTs of the current strains to obtain the FTs of the stresses generated by the current trial solution. The inverse FFT is then used to calculate the stresses generated by the current trial solution in real space. By performing these convolutions in the frequency domain the cost of calculating the trial stresses can be reduced from $O(N^2)$ to $O(N \log N)$ operations. These stresses are then used to calculate the next trial solution by applying the appropriate boundary conditions or ensuring that the next trial solution satisfies the specified constitutive relation.

If the FFT is used to calculate the trial stresses then the iterative procedure that can be implemented can only adjust the trial solution at a particular node based on the other nodal values at previous iterations (e.g. Jacobi iteration). It is not possible to make adjustments to the trial solution at a particular node based on the most up-to-date values at other nodes as is done in the Gauss–Seidel iteration. In the next section we discuss some iterative algorithms that can be developed using the FFT.

The point Fourier kernels

We now introduce a novel enhancement of the FFT approach which carries it beyond an efficient algebraic process for performing convolution products. The key feature of this enhancement is the calculation of the analytic Fourier transforms of the singular kernels in (2). These analytic frequency domain representations of the singular kernels are referred to as the "point Fourier kernels". A novel discretization of the integral equations is then achieved by sampling the analytic point Fourier kernels at discrete uniformly distributed frequencies. This new approach also allows the standard piecewise polynomial approximation schemes to be implemented within the same formulation in a way which does not necessitate the tedious integrations that are required to implement these approximation schemes in the spatial domain.

The simplest way of deriving the point Fourier kernels is to use the harmonic–biharmonic potential representation of the kernels given in Appendix A. In 3-D the FT of the harmonic potential $\Phi(r) = 1/r$ is (see Appendix B):

$$\hat{\Phi}(r) = \frac{4\pi}{\rho^2}; \quad \text{where } \rho = \sqrt{\omega_1^2 + \omega_2^2 + \omega_3^2}, \tag{18a}$$

while the FT of the biharmonic potential $\Psi(r) = r$ is:

$$\hat{\Psi}(r) = \frac{-8\pi}{\rho^4}. \tag{18b}$$

The point Fourier kernels $\hat{g}$, $\hat{G}$, $\hat{\gamma}$ and $\hat{\Gamma}$ can now be obtained by taking the appropriate derivatives of Φ and Ψ in the frequency domain. A complete listing of the point Fourier kernels $\hat{\Gamma}$ is given by Appendix B. These kernels are obtained by multiplying the potentials $\hat{\Phi}$ and $\hat{\Psi}$ by the appropriate factors of the form $i\omega_k$ according to the differentiation property for FTs [see property (FT P1)]. Each of these derivatives is unique up to a constant factor. From (9) we see that the constant factors only affect the strength of the kernels at the source point. This arbitrariness introduced by the constant factors can be resolved by exploiting the fact that the self-effect should equilibrate with the stresses generated by the source throughout the remainder of the volume. Self-equilibrating kernels can be conveniently generated in the frequency domain by exploiting the averaging property of FTs [see property (FT P8)]. For example, if we set the DC term $\hat{\Gamma}_{klmn}(\omega_j = 0) = 0$ then the stresses generated by the point strain source will equilibrate along the line x_j.

The 2-D plane strain kernels can be obtained from the 3-D kernels by integrating them along the infinite line $-\infty < z < \infty$. This process can be performed particularly simply in the frequency domain by exploiting (FT P8). Indeed, the 2-D plane strain point Fourier kernels can be obtained from the 3-D point kernels by setting $\omega_3 = 0$. For the model crack problem (17a) the appropriate point kernel can be obtained from the 2-D point Fourier kernels by using the FT inversion formula (3b) to invert the ω_2 component of $\hat{\Gamma}_{2222}(\omega_1, \omega_2)$ and setting $y = 0$:

$$\int_{-\infty}^{\infty} \frac{\exp[-(i\omega x)]}{x^2}\, dx = -\pi|\omega| = \hat{K}(\omega). \tag{19}$$

Making use of these point kernels in the iterative solution procedure in Fig. 5 we obtain the point kernel solution of the crack problem shown in Fig. 4a. The point kernel solution $u_{\text{Pt},n}$ is noticeably more accurate than the piecewise constant solution $u_{\text{PWC},n}$. In Fig. 4b we plot the point kernel approximate normalized stress profile generated by the crack along $y = 0$, $x > l$. We notice that the point kernel stresses oscillate about the analytic values. These oscillations are due to the Gibbs effect that results from the fact that a discontinuous function (17d) is represented by a finite number of Fourier modes. One way to reduce Gibbs oscillations in Fourier approximations is to introduce filters to damp the high-frequency components of the approximate solution. This procedure leads to new classes of approximations based on the FFT and will be explored shortly.

Interpolation using the FFT

It is possible to use the FFT to interpolate the approximate solution for points that do not fall on the original mesh. For example, the stresses at points not on the original mesh are obtained by assuming that the stess is a band-limited function and by interpolating using the convolution representation (5). This representation can be implemented particularly simply in the frequency domain by padding the FFT $\tilde{\sigma}_n$ of σ_k with Q zeros and taking the inverse FFT. The spatial representation then has Q additional values which fall between the points of the original solution mesh. In Fig. 6 we plot the interpolated stress values along the line segment $y = 0$, $0 \leq x \leq 2l$. We notice that the band-limited trigonometric

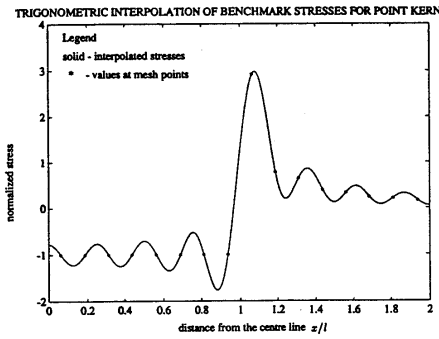

Fig. 6. The approximate stress values along the line segment $y = 0$, $0 \leqslant x \leqslant 2l$ obtained by trigonometric interpolation using the FFT. We notice that the band-limited trigonometric interpolant of the approximate point stress intensities is too oscillatory to give useful stress intensities at intermediate points.

interpolant of the approximate point stress intensities is too oscillatory to give useful stress intensities at intermediate points. However, other interpolants can be constructed in which these oscillations are damped. For example, rather than multiplying $\tilde{\sigma}_n$ by the box cut-off $b(\omega_n, 2\pi/\Delta)$ as in the case of the band-limited interpolation, we could multiply $\tilde{\sigma}_n$ by a triangular hat cut-off $h(\omega_n, \pi/\Delta)$ which will result in a less oscillatory interpolant.

Filtered kernels

In this section we show how to smooth the Gibbs oscillations by means of filters which reduce the high-frequency components of the approximate solution. Implicit in the application of a high-frequency filter to the point Fourier kernels is an assumption about the basis functions used to represent the solution in the spatial domain. Conversely, a desired form of basis function can be implemented in the frequency domain by application of the appropriate filter. We demonstrate that the standard piecewise polynomial approximations as well as a number of new approximation schemes can be obtained by filtering.

In the section on the Fourier transform we saw that the Gibbs phenomenon was associated with a slow rate of decay of the Fourier amplitudes of a function as ω increases. We try to avoid these undesirable oscillations by introducing approximate schemes that have stress components that decay more rapidly. Therefore in order to remove the oscillations in the point kernel stress approximation we multiply the point Fourier kernel $\hat{K}(\omega)$ defined in (19) by a "low pass" filter $\hat{\phi}(\omega)$ which leaves the low-frequency components unchanged but which damps the high-frequency components. Multiplying the point frequency kernel $\hat{K}(\omega)$ by a filter is a convolution in the spatial domain which is a smoothing process as we saw in the derivation of the FT of the triangular hat: $\hat{h}(\omega, \Delta)$ (13). There are a variety of filters that can be implemented and we shall introduce them by way of example.

The Lanczos filter—piecewise constants. In this case we let $\hat{\phi}(\omega) = \hat{b}(\omega, \Delta)/\Delta$ where $\hat{b}(\omega, \Delta)$ is the FT of the box function given in (10b). We note that the filter $\hat{\phi}(\omega)$ reproduces the low-frequency components, since for small ω we have

$$\hat{\phi}(\omega) \overset{\omega \to 0}{=} 1 - \tfrac{1}{6}(|\omega|\Delta/2)^2 + O[(|\omega|\Delta/2)^4]$$

while the larger frequencies are damped by a factor

$$\phi(\omega) \overset{\omega \to \infty}{=} O(1/\omega).$$

The filtered kernel becomes:

$$\hat{K}_b(\omega) = \hat{K}(\omega)\hat{\phi}(\omega) = \frac{-2\pi}{\Delta}\sin\left(\frac{|\omega|\Delta}{2}\right) \quad (20a)$$

In Fig. 7a a number of filtered kernels that will be introduced in the course of this section are compared with the point Fourier kernel. All the filters do not appreciably alter the low-frequency components (i.e. $0 < \omega/\pi < 1/2$) of the point kernels. The Lanczos filtered kernel (20a) introduces moderate damping of the high-frequency components $1/2 < \omega/\pi < 1$. In Fig. 7b the approximate normalized stresses (along $y = 0$, $x > l$) corresponding to the range of filtered kernels in Fig. 7a are plotted together with the point kernel and the analytic stresses (17d). We observe that the Lanczos filtered approximate solution does not have the stress oscillations characteristic of the point kernel so that the filter has been effective in removing the stress oscillations. In Fig. 7c the filtered approximate DD distributions are plotted together with the point kernel approximate and the analytic solution (17c). We observe that the Lanczos filter approximate is slightly less accurate than the point kernel approximate at the centre of the crack and is somewhat less accurate near the crack tip.

In order to interpret (20a) (and the performance of the Lanczos approximate shown in Fig. 7b,c) we observe that by applying the Fourier series of the form (4a) to

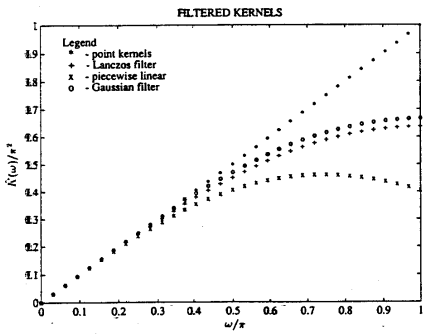

Fig. 7a. The point Fourier kernels (19) and the Lanczos, piecewise linear, and Gaussian filtered kernels in the frequency domain.

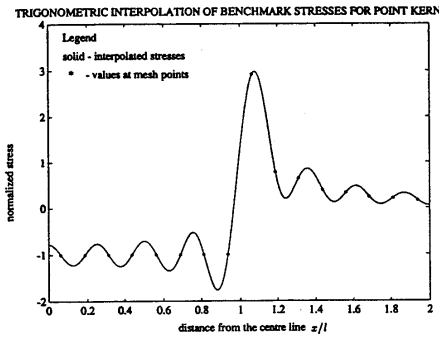

Fig. 6. The approximate stress values along the line segment $y = 0$, $0 \leqslant x \leqslant 2l$ obtained by trigonometric interpolation using the FFT. We notice that the band-limited trigonometric interpolant of the approximate point stress intensities is too oscillatory to give useful stress intensities at intermediate points.

interpolant of the approximate point stress intensities is too oscillatory to give useful stress intensities at intermediate points. However, other interpolants can be constructed in which these oscillations are damped. For example, rather than multiplying $\tilde{\sigma}_n$ by the box cut-off $b(\omega_n, 2\pi/\Delta)$ as in the case of the band-limited interpolation, we could multiply $\tilde{\sigma}_n$ by a triangular hat cut-off $h(\omega_n, \pi/\Delta)$ which will result in a less oscillatory interpolant.

Filtered kernels

In this section we show how to smooth the Gibbs oscillations by means of filters which reduce the high-frequency components of the approximate solution. Implicit in the application of a high-frequency filter to the point Fourier kernels is an assumption about the basis functions used to represent the solution in the spatial domain. Conversely, a desired form of basis function can be implemented in the frequency domain by application of the appropriate filter. We demonstrate that the standard piecewise polynomial approximations as well as a number of new approximation schemes can be obtained by filtering.

In the section on the Fourier transform we saw that the Gibbs phenomenon was associated with a slow rate of decay of the Fourier amplitudes of a function as ω increases. We try to avoid these undesirable oscillations by introducing approximate schemes that have stress components that decay more rapidly. Therefore in order to remove the oscillations in the point kernel stress approximation we multiply the point Fourier kernel $\hat{K}(\omega)$ defined in (19) by a "low pass" filter $\hat{\phi}(\omega)$ which leaves the low-frequency components unchanged but which damps the high-frequency components. Multiplying the point frequency kernel $\hat{K}(\omega)$ by a filter is a convolution in the spatial domain which is a smoothing process as we saw in the derivation of the FT of the triangular hat: $\hat{h}(\omega, \Delta)$ (13). There are a variety of filters that can be implemented and we shall introduce them by way of example.

The Lanczos filter—piecewise constants. In this case we let $\hat{\phi}(\omega) = \hat{b}(\omega, \Delta)/\Delta$ where $\hat{b}(\omega, \Delta)$ is the FT of the box function given in (10b). We note that the filter $\hat{\phi}(\omega)$ reproduces the low-frequency components, since for small ω we have

$$\hat{\phi}(\omega) \overset{\omega \to 0}{=} 1 - \tfrac{1}{6}(|\omega|\Delta/2)^2 + O[(|\omega|\Delta/2)^4]$$

while the larger frequencies are damped by a factor

$$\phi(\omega) \overset{\omega \to \infty}{=} O(1/\omega).$$

The filtered kernel becomes:

$$\hat{K}_b(\omega) = \hat{K}(\omega)\hat{\phi}(\omega) = \frac{-2\pi}{\Delta}\sin\left(\frac{|\omega|\Delta}{2}\right) \quad (20a)$$

In Fig. 7a a number of filtered kernels that will be introduced in the course of this section are compared with the point Fourier kernel. All the filters do not appreciably alter the low-frequency components (i.e. $0 < \omega/\pi < 1/2$) of the point kernels. The Lanczos filtered kernel (20a) introduces moderate damping of the high-frequency components $1/2 < \omega/\pi < 1$. In Fig. 7b the approximate normalized stresses (along $y = 0$, $x > l$) corresponding to the range of filtered kernels in Fig. 7a are plotted together with the point kernel and the analytic stresses (17d). We observe that the Lanczos filtered approximate solution does not have the stress oscillations characteristic of the point kernel so that the filter has been effective in removing the stress oscillations. In Fig. 7c the filtered approximate DD distributions are plotted together with the point kernel approximate and the analytic solution (17c). We observe that the Lanczos filter approximate is slightly less accurate than the point kernel approximate at the centre of the crack and is somewhat less accurate near the crack tip.

In order to interpret (20a) (and the performance of the Lanczos approximate shown in Fig. 7b,c) we observe that by applying the Fourier series of the form (4a) to

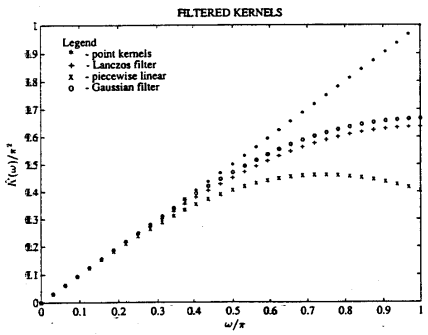

Fig. 7a. The point Fourier kernels (19) and the Lanczos, piecewise linear, and Gaussian filtered kernels in the frequency domain.

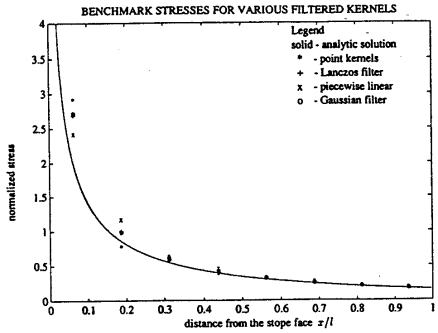

Fig. 7b. The analytic normalized stress distribution (17d) ahead of the crack-like excavation and the corresponding point Fourier, Lanczos, piecewise linear and Gaussian filter approximates. All the filter approximates remove the Gibbs oscillations.

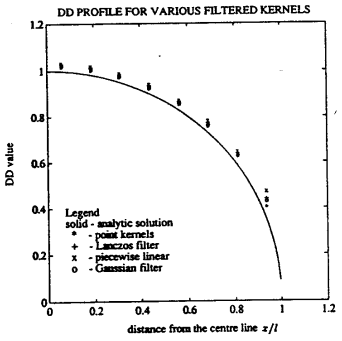

Fig. 7c. The analytic DD distribution (17c) in the case $p(x) = \gamma$ and the corresponding point Fourier, Lanczos, piecewise linear and Gaussian filter approximate solutions.

the infinite extension of the piecewise constant kernel defined in (17b) we obtain:

$$\bar{A}(\omega) = \frac{\gamma}{\pi\Delta} \sum_{m=-\infty}^{\infty} \frac{\exp(-i\omega m\Delta)}{m^2 - \frac{1}{4}}$$

$$= \frac{\gamma}{\pi}\left[\frac{-2\pi}{\Delta}\sin\left(\frac{|\omega|\Delta}{2}\right)\right]. \qquad (20a')$$

Thus comparing (20a) with (20a') we see that by applying the Lanczos filter to the point kernel $\hat{K}(\omega)$ we will obtain precisely the frequency representation of the piecewise constant kernel given in (17b). Therefore, a piecewise constant representation of the solution can be obtained (without having to perform spatial integrations) by applying a Lanczos filter to the point kernel. This is not surprising since we used a filter $\hat{\phi}(\omega)$ that was the Fourier transform of the box function—the basis function for piecewise constants. This simple example not only illustrates the possibility of preparing the piecewise constant kernels in the frequency domain but it also raises the possibility of preparing other classes of approximation schemes by implementing the FTs of their basis functions as filters.

The linear spline filter. In this case we let $\hat{\phi}(\omega) = \hat{h}(\omega, \Delta)/\Delta$ where $\hat{h}(\omega, \Delta)$ is the FT of the triangular hat function given in (13b). We note that this filter $\hat{\phi}(\omega)$ multiplies the low-frequency components by the factor

$$\hat{\phi}(\omega) \overset{\omega\to 0}{=} 1 - \tfrac{1}{3}(|\omega|\Delta/2)^2 + O[(|\omega|\Delta/2)^4]$$

while the larger frequencies are damped by a factor

$$\hat{\phi}(\omega) \overset{\omega\to\infty}{=} O(1/\omega^2).$$

The filtered kernel is given by:

$$\hat{K}_h(\omega) = \hat{K}(\omega)\hat{\phi}(\omega) = \frac{-4\pi\sin^2\left(\frac{|\omega|\Delta}{2}\right)}{\Delta^2|\omega|}. \qquad (20b)$$

From Fig. 7a it can be seen that the piecewise linear filter substantially reduces the high-frequency components of the point kernels. From Fig. 7b we observe that the linear spline filter removes the oscillations displayed by the point kernel stresses. The piecewise linear approximate is more accurate than the others for the benchmark stress closest to the fact but is less accurate than the other approximates for the remaining benchmarks further ahead of the face. From Fig. 7c we see that the linear spline filter approximate DD distribution is slightly less accurate than the point kernel approximate. Therefore, for the model crack problem, the continuous linear spline approximate does not offer any improvement over the piecewise constant solution—a result which has already been established [13]. We note that the piecewise linear approximation scheme is extremely simple to implement in the frequency domain and requires only $O(N)$ additional operations. In order to implement this scheme in the spatial domain, we would have to derive a whole new set of discrete kernels involving the evaluation of singular integrals—these calculations are even more severe for fully 2- and 3-D geometries.

The poor performance of the piecewise linear approximation is due to the rather extreme behaviour of the analytic solution of the model crack problem in the neighbourhood of the endpoints $\pm l$, i.e.

$$U(x) \overset{x\to l}{\sim} p\sqrt{2l}\sqrt{l - x/\gamma}.$$

In the frequency domain this extreme behaviour manifests itself in the $O(1/\omega^{3/2})$ decay of the FT of the analytic solution [see (17c)]. The piecewise linear basis functions implicitly assume that the solution is smoother in that the frequency components are assumed to decay at a rate $O(1/\omega^2)$. For this reason the piecewise linear representation has difficulty capturing the slower $[O(1/\omega^{3/2})]$ decaying coefficients of the analytic solution. We see, therefore, that there is little benefit for this particular problem in trying to implement higher order

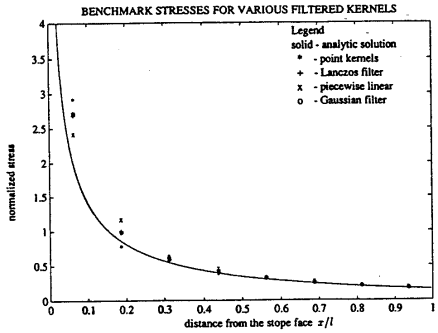

Fig. 7b. The analytic normalized stress distribution (17d) ahead of the crack-like excavation and the corresponding point Fourier, Lanczos, piecewise linear and Gaussian filter approximates. All the filter approximates remove the Gibbs oscillations.

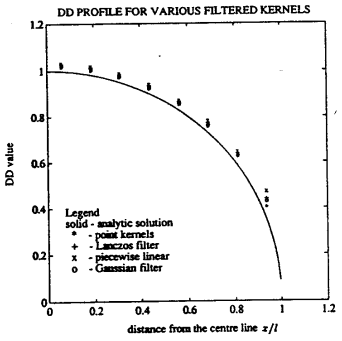

Fig. 7c. The analytic DD distribution (17c) in the case $p(x) = \gamma$ and the corresponding point Fourier, Lanczos, piecewise linear and Gaussian filter approximate solutions.

the infinite extension of the piecewise constant kernel defined in (17b) we obtain:

$$\bar{A}(\omega) = \frac{\gamma}{\pi\Delta} \sum_{m=-\infty}^{\infty} \frac{\exp(-i\omega m\Delta)}{m^2 - \frac{1}{4}}$$

$$= \frac{\gamma}{\pi}\left[\frac{-2\pi}{\Delta}\sin\left(\frac{|\omega|\Delta}{2}\right)\right]. \qquad (20a')$$

Thus comparing (20a) with (20a') we see that by applying the Lanczos filter to the point kernel $\hat{K}(\omega)$ we will obtain precisely the frequency representation of the piecewise constant kernel given in (17b). Therefore, a piecewise constant representation of the solution can be obtained (without having to perform spatial integrations) by applying a Lanczos filter to the point kernel. This is not surprising since we used a filter $\hat{\phi}(\omega)$ that was the Fourier transform of the box function—the basis function for piecewise constants. This simple example not only illustrates the possibility of preparing the piecewise constant kernels in the frequency domain but it also raises the possibility of preparing other classes of approximation schemes by implementing the FTs of their basis functions as filters.

The linear spline filter. In this case we let $\hat{\phi}(\omega) = \hat{h}(\omega, \Delta)/\Delta$ where $\hat{h}(\omega, \Delta)$ is the FT of the triangular hat function given in (13b). We note that this filter $\hat{\phi}(\omega)$ multiplies the low-frequency components by the factor

$$\hat{\phi}(\omega) \overset{\omega\to 0}{=} 1 - \tfrac{1}{3}(|\omega|\Delta/2)^2 + O[(|\omega|\Delta/2)^4]$$

while the larger frequencies are damped by a factor

$$\hat{\phi}(\omega) \overset{\omega\to\infty}{=} O(1/\omega^2).$$

The filtered kernel is given by:

$$\hat{K}_h(\omega) = \hat{K}(\omega)\hat{\phi}(\omega) = \frac{-4\pi\sin^2\left(\frac{|\omega|\Delta}{2}\right)}{\Delta^2|\omega|}. \qquad (20b)$$

From Fig. 7a it can be seen that the piecewise linear filter substantially reduces the high-frequency components of the point kernels. From Fig. 7b we observe that the linear spline filter removes the oscillations displayed by the point kernel stresses. The piecewise linear approximate is more accurate than the others for the benchmark stress closest to the fact but is less accurate than the other approximates for the remaining benchmarks further ahead of the face. From Fig. 7c we see that the linear spline filter approximate DD distribution is slightly less accurate than the point kernel approximate. Therefore, for the model crack problem, the continuous linear spline approximate does not offer any improvement over the piecewise constant solution—a result which has already been established [13]. We note that the piecewise linear approximation scheme is extremely simple to implement in the frequency domain and requires only $O(N)$ additional operations. In order to implement this scheme in the spatial domain, we would have to derive a whole new set of discrete kernels involving the evaluation of singular integrals—these calculations are even more severe for fully 2- and 3-D geometries.

The poor performance of the piecewise linear approximation is due to the rather extreme behaviour of the analytic solution of the model crack problem in the neighbourhood of the endpoints $\pm l$, i.e.

$$U(x) \overset{x\to l}{\sim} p\sqrt{2l}\sqrt{l - x/\gamma}.$$

In the frequency domain this extreme behaviour manifests itself in the $O(1/\omega^{3/2})$ decay of the FT of the analytic solution [see (17c)]. The piecewise linear basis functions implicitly assume that the solution is smoother in that the frequency components are assumed to decay at a rate $O(1/\omega^2)$. For this reason the piecewise linear representation has difficulty capturing the slower $[O(1/\omega^{3/2})]$ decaying coefficients of the analytic solution. We see, therefore, that there is little benefit for this particular problem in trying to implement higher order

spline approximations as they will assume that the solution is even smoother. There may well be some merit in using higher order variations in situations where the solution is not expected to change as abruptly as it does in the case of a crack-like excavation.

Gaussian filters. We now introduce a new class of approximation schemes which were first introduced in vortex dynamics [14]. This class of approximation schemes allows some flexibility in the extent to which the low frequencies are reproduced and the high frequencies are damped. To reproduce the low frequencies faithfully we would like $\hat{\phi}(\omega) = 1$ on a large interval containing $\omega = 0$. Therefore, to ensure that $\hat{\phi}(\omega)$ be as flat as possible we impose the following two constraints:

(i) $\hat{\phi}(0) = 1$,

(ii) $d^k\hat{\phi}(\omega)/d\omega^k]_{\omega=0} = 0; \quad k = 1, \ldots, 2p.$

We note that these constraints are equivalent in the spatial domain to the following moment conditions:

(i′) $\int_{-\infty}^{\infty} \phi(x)\,dx = 1$,

(ii′) $\int_{-\infty}^{\infty} x^k\phi(x)\,dx = 0; \quad k = 1, \ldots, 2p.$

In order to have the freedom to satisfy these constraints we construct $\hat{\phi}(\omega)$ as a linear combination of dilated Gaussians (i.e. Gaussians that are made to vary on a number of different length scales). As the basic building block consider the Gaussian [see (14)]:

$$\psi(x) = g(x, 1) = \frac{\exp(-x^2)}{\sqrt{\pi}}; \quad \hat{\psi}(x) = \exp\left(-\left(\frac{\omega}{2}\right)^2\right)$$

and assume the following expansion for the filter $\phi^{(2p)}$:

$$\phi^{(2p)}(x) = \sum_{i=1}^{p} c_i\psi\left(\frac{x}{a_i}\right), \tag{21a}$$

where c_i are coefficients used to ensure that $\phi^{(2p)}(x)$ satisfies the moment conditions and a_i are the user-defined parameters that adjust the length scales of the dilated Gaussians. Since ψ is an even function, the odd moment conditions in (ii′) are satisfied automatically. The even moment conditions yield the following system of equations:

$$\delta_{k1} = \sum_{i=1}^{p} c_i a_i^{2k+1}; \quad k = 1, \ldots, p;$$

where

$$\delta_{ij} = \begin{cases} 0, & i \neq j, \\ 1, & i = j, \end{cases}$$

from which the coefficients c_i can be determined.

In order to adjust the rate of decay of the filter we define the one-parameter family of rescaled filters:

$$\phi_\delta^{(2p)}(x) = \frac{1}{\delta}\phi^{(2p)}\left(\frac{x}{\delta}\right). \tag{21b}$$

We now have an adaptable class of approximations. If the low frequencies are to be reproduced faithfully then p is increased and if the high frequencies are to be damped more rapidly then δ is increased [since $\mathcal{F}\{\phi_\delta^{(2p)}\} = \hat{\phi}^{(2p)}(\delta\omega)$].

The Gaussian filter shown in Fig. 7a has defining parameters $p = 4$, $\delta = 28\Delta$ and $a_i = (\frac{1}{2})^{i-1}$. This filter faithfully reproduces the low-frequency components while it reduces the high-frequency components slightly less than the Lanczos filter. The Gaussian approximate stresses shown in Fig. 7b do not have the oscillations displayed by the point kernel approximate and are as accurate as the Lanczos approximation stresses. The Gaussian approximate shown in Fig. 7c achieves roughly the same superior accuracy for the DD distribution as does the point kernel approximate.

Consequences of the periodicity constraint of the FFT

In this section we discuss the constraint imposed by the periodic assumption of the FFT approach and some techniques that can be used to reduce its effect. In addition, we discuss the advantages of the FFT approach when we wish to model periodically repeated problems.

Avoiding the periodic assumption. We saw in the section on the Fourier transform that the discrete Fourier transform assumes that the sequences are periodic. Although this situation does arise in practical mining problems (e.g. a periodic array of pillars), it is generally not true that the solutions we seek are periodic. Therefore we discuss ways to solve non-periodic problems by embedding them within equivalent but larger periodic problems. Broadly speaking we extend the region on which the problem is defined to a larger one in which the additional parts of the larger domain act as cushions against the errors introduced by the periodicity assumption of the FFT.

In order to illustrate this process consider (17b) in which $N = 4$ and $\gamma/\pi\Delta = 1$. In this case the influence matrix A is:

$$A = \begin{bmatrix} -4 & 4/3 & 4/15 & 4/35 \\ 4/3 & -4 & 4/3 & 4/15 \\ 4/15 & 4/3 & -4 & 4/3 \\ 4/35 & 4/15 & 4/3 & -4 \end{bmatrix}. \tag{22}$$

We note that the matrix A has a Toeplitz structure in that the elements along each diagonal are constant. Since A is also symmetric, it can be defined by merely listing the elements of the first row. These properties can be expressed as follows: $A_{mn} = a_{|m-n|}$, where a_n is an element of the sequence $\{a_n\}_0^{N-1} = \{-4, 4/3, 4/15, 4/35\}$. As a result of this Toeplitz structure, (17b) can be written in the form of a discrete convolution:

$$(a * u)_n = \sum_{m=1}^{N} a_{|n-m|}u_m = f_n. \tag{23}$$

If we extend the sequence $\{a_n\}$ to one which is N-periodic then we will be able to evaluate the convolution (23) in $O(N \log N)$ operations using the FFT as

opposed to the $O(N^2)$ operations required to evaluate the convolution directly. Direct periodic extension of $\{a_n\}$ to a sequence $\{a'_n: a'_{n+pN} = a_n\}$ does not yield a sequence with the correct symmetry properties $a'_n = a'_{-n}$. Therefore, to take advantage of the efficiency of the FFT we must extend the sequence to a new sequence which is both N-periodic and symmetric e.g.:

$$\{a'_n\}_0^{2N-1} =$$
$$\{-4,\ 4/3,\ 4/15,\ 4/35,\ 4/63,\ 4/35,\ 4/15,\ 4/3\}$$

We now consider the following product of the Toeplitz matrix A' associated with this sequence and the vector u' constructed from u by padding with zeros:

$$A'u' = \begin{bmatrix} -4 & 4/3 & 4/15 & 4/35 & 4/63 & 4/35 & 4/15 & 4/3 \\ 4/3 & -4 & 4/3 & 4/15 & 4/35 & 4/63 & 4/35 & 4/15 \\ 4/15 & 4/3 & -4 & 4/3 & 4/15 & 4/35 & 4/63 & 4/35 \\ 4/35 & 4/15 & 4/3 & -4 & 4/3 & 4/15 & 4/35 & 4/63 \\ 4/63 & 4/35 & 4/15 & 4/3 & -4 & 4/3 & 4/15 & 4/35 \\ 4/35 & 4/63 & 4/35 & 4/15 & 4/3 & -4 & 4/3 & 4/15 \\ 4/15 & 4/35 & 4/63 & 4/35 & 4/15 & 4/3 & -4 & 4/3 \\ 4/3 & 4/15 & 4/35 & 4/63 & 4/35 & 4/15 & 4/3 & -4 \end{bmatrix} \begin{bmatrix} 0 \\ 0 \\ u_1 \\ u_2 \\ u_3 \\ u_4 \\ 0 \\ 0 \end{bmatrix} = \begin{bmatrix} \times \\ \surd \\ \surd \\ \surd \\ \surd \\ \surd \\ \surd \\ \times \end{bmatrix}. \tag{24}$$

In addition to being a Toeplitz matrix, A' has an additional special structure in that successive rows (or columns) are cyclic permutations of one another. Such a Toeplitz matrix is known as a circulant matrix. We note that multiplication by the circulant matrix A' in (24) yields the same result as multiplication in the frequency domain by the FT of the sequence $\{a'_n\}_0^{2N-1}$. To see this consider the product of A' with the elements of the Fourier basis:

$$\sum_{m=0}^{2N-1} a'_{n-m} \exp[2\pi imk/(2N)]$$
$$= \exp[2\pi ink/(2N)] \times \sum_{m=0}^{2N-1} a'_{n-m} \exp[-2\pi i(n-m)k/(2N)]$$
$$= (2N)\tilde{a}'_k \exp[2\pi ink/(2N)].$$

Thus the eigenvalues of the circulant matrix A' are just the FFT components $\tilde{a}'_k$ of the sequence $\{a'_n\}_0^{2N-1}$. Now using the convolution property (FFT P2) of the FFT we obtain the desired result:

$$A'u' = \mathrm{FFT}^{-1}\{\tilde{a}'_k u'_k\}.$$

The matrix represenation (24) of the action of the FFT convolution enables us to easily verify the effect of extending $\{a_n\}$. By using the FFT of the extended sequence we see from (24) that we obtain correct stresses at the points ($\surd$) and errors of $(4/35-4/99)u_4$ in the stresses at the points ($\times$) due to periodic wraparound. If we only wish to solve for the unknowns $u_1, \ldots, u_4$ iteratively then this extension process is quite adequate since the correct tractions will be calculated at the collocation points. Alternatively, if we defined the extended solution vector u' to be:

$$u' = [u_1\ u_2\ u_3\ u_4\ 0\ 0\ 0\ 0],$$

then we would still calculate correct tractions at positions $1, \ldots, 5$ but the errors in the stresses calculated in positions $6, \ldots, 8$ would be substantially larger due to the closer proximity of the periodically repeated cracks. Therefore, if the benchmark stresses generated by the FFT are to be used as estimates of the true stresses then it is preferable to locate the excavations in the centre of the padded region. This situation is analogous to the errors which occur when the remote boundaries are located too close in finite difference or finite element analyses.

A scheme proposed by Stewart [11] to calculate more accurate benchmark stresses using the FFT convolution approach involves padding the sequence $\{a'_n\}$ with N zeros:

$$\{a'_n\}_0^{3N-1} = \{-4,\ 4/3,\ 4/15,\ 4/35,\ 4/63,\ 0,$$
$$0,\ 0,\ 0,\ 4/35,\ 4/15,\ 4/3\}.$$

By constructing the associated circulant matrix for this sequence it can be seen that the wraparound errors in the benchmark stresses are substantially reduced.

Exploiting the periodicity for repeating geometries. In this section we see that the FFT can be used to model an infinitely repeating sequence of excavations such as those that arise in repeated pillar geometries.

Infinitely repeating mining geometries—analytic solution and classic replicating kernels. Consider a repeated pillar situation modelled by an infinite sequence of crack-like excavations with spacing $2L$, each having a span of $2l$ and subjected to a boundary traction $p(x) = p =$ constant. In this case the analytic solution [analogous to (17c)] is as follows [15]:

$$U(x) = \frac{2Lp}{\pi\gamma} \cosh^{-1}\left[\cos\left(\frac{\pi x}{2L}\right) \Big/ \cos\left(\frac{\pi l}{2L}\right)\right]. \tag{25}$$

In the case of an infinitely repeating crack-like excavation, the discretized equation (47) is of the form:

$$\sum_{m=-\infty}^{\infty} a_{n-m} u_m = f_n. \tag{26a}$$

Let the geometry repeat itself after N meshpoints so that $u_{m+kN}=u_m$. Now, making use of the identity $\Sigma_{n=-\infty}^{\infty} Q_n = \Sigma_{p=-\infty}^{\infty} \Sigma_{q=1}^{N} Q_{q-pN}$ (which applies for any infinite sum) and the N-periodicity of u_n, we can rewrite (26a) in the following form:

$$f_n = \sum_{m=1}^{N} u_m \left\{ \sum_{p=-\infty}^{\infty} a_{n+pN-m} \right\} = \sum_{m=1}^{N} \alpha_{n-m} u_m,$$

where α_n is the aliased or replicating kernel defined by $\alpha_n = \Sigma_{p=-\infty}^{\infty} a_{n+pN}$. Thus we can reduce the infinite problem (26a) to a finite one in which the replicating kernel α_n represents the stresses generated by an infinite array of DDs of unit magnitude. This sum can be evaluated analytically [16, 17] to yield:

$$\alpha_n = \sum_{p=-\infty}^{\infty} \frac{1}{(n+pN)^2 - \frac{1}{4}}$$

$$= \frac{\pi \sin \pi/N}{N \sin \pi(n-\frac{1}{2})/N \sin \pi(n+\frac{1}{2})/N}. \quad (26b)$$

We note that as the length N of the period becomes larger, the influence of the periodically repeated DDs becomes less so that:

$$\alpha_n \overset{N\to\infty}{=} \frac{1}{n^2-\frac{1}{4}} + \frac{1}{3}\left(\frac{\pi}{N}\right)^2 + O\left(\frac{1}{N^4}\right) \overset{N\to\infty}{\longrightarrow} a_n.$$

Generating replicating kernels by means of the FFT. In this section we demonstrate how discretizations based on generating kernels in the frequency domain using the FFT naturally lead to aliased or replicating kernels. For the purposes of this demonstration we consider the point kernel (19), however, the same results apply to any of the filtered kernels discussed above.

Let us review in detail the procedure followed to arrive at the point kernel approach:

Step 1. Analytic calculation of the Fourier transform:

$$K(x) = \frac{1}{|x|^2} \overset{\text{FT}}{\longrightarrow} \hat{K}(\omega) = -\pi|\omega|.$$

Step 2. Approximate $K(x)$ by a function $k(x_n)$ having a periodically repeating FT. We build $k(x_n)$ by assuming $\bar{k}(\omega) = -\pi|\omega|$ for $-\pi/\Delta < \omega < \pi/\Delta$ and $\bar{k}(\omega + 2\pi/\Delta) = \bar{k}(\omega)$. Making use of the inversion formula (4b) we obtain:

$$k(x_n) = \int_{-\pi/\Delta}^{\pi/\Delta} -\pi|\omega| \exp(i\omega x_n) \frac{d\omega}{2\pi}$$

$$= \frac{\pi^2}{2\Delta^2} \frac{\sin^2(\pi n/2)}{(\pi n/2)^2} \quad (27a)$$

and by the formula (4a) we have:

$$\bar{k}(\omega) = \Delta \sum_{q=-\infty}^{\infty} k(x_q) \exp(-i\omega k_q). \quad (27b)$$

Step 3. Use the FFT to determine the approximate kernel κ_p. We arrive at the kernel κ_n by sampling $\bar{k}(\omega)$ at the N discrete frequencies $\omega_n = 2\pi n/N\Delta$: $n = 0, \ldots, N-1$:

$$\kappa_p = \sum_{n=0}^{N-1} \bar{k}(\omega_n) \exp(2\pi i n p/N)$$

$$= \sum_{n=0}^{N-1} \left\{ \Delta \sum_{q=-\infty}^{\infty} k(x_q) \exp(-2\pi i n q/N) \right\} \times \exp(2\pi i n p/N)$$

$$= \sum_{q=-\infty}^{\infty} k(x_q) \left\{ \frac{1}{N} \sum_{n=0}^{N-1} \exp[2\pi i n (p-q)/N] \right\}$$

$$= \sum_{q=-\infty}^{\infty} k(x_{p+qN}), \quad (28)$$

where the identity (7b) has been used.

From (28) we see that the kernel κ_p generated by the FFT is just the aliased version of the discrete kernel $k(x_n)$ given in (27a). Thus the FFT can be used to generate a set of aliased or replicating kernels automatically by sampling, at a finite number of frequencies, the continuous FT of the kernels that are to be replicated. We note that in the derivation of (28) none of the detailed properties of the kernel $k(x_n)$ used in this illustration were used so that (28) applies to all such kernels generated by sampling the continuous FT (e.g. the filtered kernels discussed above).

In Fig. 8a we plot the kernels $a'_n = a'_{N-n} = a_n$, α_n and κ_n for the case $N = 8$. Even for this small value of N we note that $\alpha_n \approx a'_n$. In Fig. 8b we plot the approximate DD distribution using: the aliased point kernel [i.e. using κ_n given in (28)] and aliased piecewise constant kernels [i.e. using α_n given in (26b)]. In addition we plot the analytic solution (25) in the infinitely repeating case as well as the analytic solution (17c) for an isolated crack-like excavation.

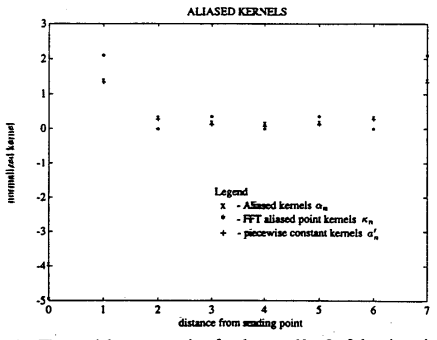

Fig. 8a. The spatial representation for the case $N = 8$ of the piecewise constant aliased kernels α_n [see (26b)], the point Fourier aliased kernels κ_n [see (28)], and for comparison the isolated symmetric piecewise constant kernels a'_n. Even for this small value of N we note that $\alpha_n \approx a'_n$.

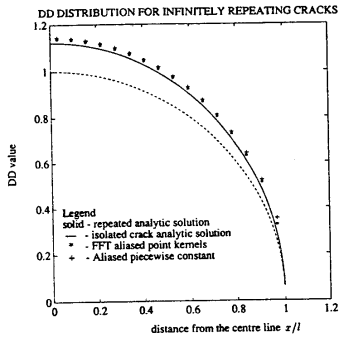

Fig. 8b. The analytic solution (25) in the infinitely repeating case as well as the analytic solution (17c) for an isolated crack-like excavation as well as the approximate DD distributions using: the aliased point kernel (i.e. using κ_n given in (28)) and aliased piecewise constant kernels (i.e. using α_n given in (26b)).

Generating non-replicating kernels in the frequency domain. Since the frequency domain preparation of the kernels automatically constructs replicating kernels, it is natural to try to generate the kernels $k(x_n)$ in the frequency domain (as opposed to the replicating kernels κ_n). This situation would arise if we wished to model a single crack-like excavation and therefore needed to suppress the replication property of the FFT.

In essence we are trying to find the FFT for the kernels we would obtain by enlarging the sequence $k(x_n)$ [see (27a)] to the sequence $k'(x_n) = k'(x_{-n}) = k'(x_{n+pN}) = k(x_n)$ and proceeding as in "Avoiding the periodic assumption". Since the kernels $k(x_n)$ are derived from special solutions of the equilibrium equations (see the second section), the stresses generated throughout the elastic body of the elemental DD should balance. As a particular consequence of this, the kernel $k(x_n)$ should self-equilibrate on the interval $-\infty < n < \infty$, i.e. $\Sigma_{q=-\infty}^{\infty} k(x_q) = 0$. As discussed previously, self-equilibration is ensured by the condition that $\bar{k}(\omega = 0) = 0$. Since the replicating kernel κ_n represents the infinite superposition of the periodically repeated influences $k(x_{n+pN})$ according to (28), it follows that the replicating kernels should self-equilibrate within one period i.e.:

$$\tilde{\kappa}_0 = \sum_{n=0}^{N-1} \kappa_n = \sum_{p=0}^{N-1} \left\{ \sum_{q=-\infty}^{\infty} k(x_{p+qN}) \right\} = 0. \qquad (29)$$

In contrast, the extended kernels $k'(x_n)$ do not self-equilibrate within a single period. In fact:

$$\tilde{k}'_0 = \sum_{n=0}^{N-1} k'(x_n) = -\sum_{|n|>N/2} k(x_n) \neq 0. \qquad (30)$$

This distinction between the replicating kernels κ_n and the non-replicating kernels $k'(x_n)$ can be used to generate the non-replicating kernels in the frequency domain. In particular, by constraining the lowest Fourier amplitude $\tilde{k}'_0$ to be equal to the tail $-\Sigma_{|n|>N/2} k(x_n)$ and letting $\tilde{k}'_n = -\pi|\omega_n|$; $n = 1, \ldots, N-1$ we can prepare the non-replicating kernels $k'(x_n)$ in the frequency domain and can, therefore, model isolate crack-like excavations.

EFFICIENT SOLUTION OF DISCRETIZED EQUATIONS

The algebraic equations to be solved

In this section we consider the efficient solution of the algebraic equations of the form:

$$Au = f + \sigma(u), \qquad (31)$$

which arise from a discretization of (17a) such as (17b). Here u contains the DD components, A is the influence matrix, f are the imposed tractions and $\sigma(u)$ are the (in general non-linear) material reactions within the DD elements. Practical situations in which non-linear material reactions occur include modelling the effect of backfill after mining and modelling a soft seam ahead of a tabular excavation.

In this section we discuss two iterative algorithms that can be used to solve the algebraic equations (31) efficiently. The first scheme exploits the fact that with the aid of the FFT we have a close approximation to the eigenvalues of the matrix A. This information enables us to construct, in the frequency domain, an approximate inverse for A in $O(N \log N)$ operations which greatly enhances the speed of the calculation. In fact the number of iterations required to arrive at a solution remains almost constant so that the asymptotic operation count for the method is $O(N \log N)$. This algorithm does, however, require the storage of three additional vectors, each as large as the solution vector u, which are not required by more traditional iterative methods such as the Jacobi method. This additional storage requirement may in some cases limit the number of degrees of freedom that can be used in the model.

The second method is an enhancement of the Jacobi iteration in which near-neighbour influences to the one being adjusted are altered to reflect the back influence of those neighbours at the next iteration step. This approach results in improved efficiency with virtually no additional memory requirements.

The spectrally preconditioned conjugate gradient method

Recently there has been considerable interest in the use of preconditioned conjugate gradient algorithms to solve systems of algebraic equations using incomplete factorizations of A [18, 19] and using circulant preconditioners for matrices with the Toeplitz structure [20]. The spectral preconditioner we advocate is constructed from the inverse of the extended matrix A' which is used to calculate the convolution products in the iteration process by means of the FFT. Since we use the same kernel matrix A' this preconditioner has the advantage that no additional memory is required. The preconditioner is constructed in the frequency domain so that the preconditioning calculation only takes $O(N \log N)$ additional operations.

The preconditioned conjugate gradient (PCG) method

Assume that we are only considering a linear problem so that $\sigma(u) = 0$. In this case the PCG algorithm can be stated as follows:

(i) *Initialization:*

Given u_0 (the initial guess)

Solve $Cz_0 = (f - Au_0) = r_0$

$d_0 = z_0$;

(ii) **for** $k = 1$ **to** N:

$$u_k = u_{k-1} + \alpha_{k-1} d_{k-1}$$

$$\text{where} \quad \alpha_{k-1} = \frac{r_{k-1}^{\mathrm{T}} d_{k-1}}{d_{k-1}^{\mathrm{T}} A d_{k-1}}, \tag{32a}$$

$$r_k = r_{k-1} - \alpha_{k-1} A d_{k-1}, \tag{32b}$$

$$\textbf{Solve} \quad Cz_k = r_k, \tag{32c}$$

$$d_k = z_k + \beta_{k-1} d_{k-1}$$

$$\text{where} \quad \beta_{k-1} = -\frac{z_k^{\mathrm{T}} A d_{k-1}}{d_{k-1}^{\mathrm{T}} A d_{k-1}}. \tag{32d}$$

Here the matrix C is the preconditioner and can be regarded as an approximate inverse of A. For Jacobi-like iteration, preconditioning can be expressed in the form:

$$u_k = u_{k-1} + C^{-1}(f - Au_{k-1}). \tag{33}$$

For the preconditioned method (33) the convergence depends on the extreme eigenvalues of $(I - C^{-1}A)$. Since $C^{-1} \approx A^{-1}$, many of the eigenvalues of $(I - C^{-1}A)$ are close to zero, but some may be larger in magnitude than 1, in which case the scheme (33) will diverge. The convergence of the PCG method on the other hand depends on the distribution of all the eigenvalues of $C^{-1}A$ and not exclusively on the extremal eigenvalues. Moreover, it can be shown that the PCG scheme (32) converges particularly rapidly when all (or a large number) of the eigenvalues of $C^{-1}A$ are clustered. In addition, the PCG method does not diverge if the extremal eigenvalues are larger than 1.

Note that the iterative scheme (32) only involves one multiplication of the form Ad so that relatively little additional computation is required provided that C can be inverted rapidly.

Constructing the spectral preconditioner C^{-1}. The question which naturally arises in the context of the FFT approach to solving (31) is whether it is possible to invert A directly in the frequency domain i.e.:

$$\tilde{u}_n = \tilde{f}_n / \tilde{A}_n. \tag{34}$$

Unfortunately this is not possible since A has to be extended (see "Avoiding the periodic assumption") to a larger matrix A' in order that the periodicity assumption imposed by the FFT does not alter the original equations (31). However, iteration with the extended matrix A' is possible since by padding u with zeros to give u' it is possible to use the FFT to calculate the required matrix products Au efficiently. Since $\tilde{f}_n'$ is not known, direct inversion by means of (34) is not possible. However, we use A' to construct an approximate inverse in the frequency domain.

The sequence of preconditioning steps [see (32c)] in $O(N \log N)$ operations is:

(1) Extend $r_k = [r_1\ r_2\ r_3\ r_4]^{\mathrm{T}}$ to

$r_k' = [0\ 0\ r_1\ r_2\ r_3\ r_4\ 0\ 0]^{\mathrm{T}}$.

(2) Calculate the FT of r_k': $r_k' \overset{\mathrm{FT}}{\rightarrow} \tilde{r}_n'$.

(3) Evaluate z_k:

$$\tilde{z}_n' = \tilde{r}_n' / \tilde{A}_n',$$

$$z_k' = \mathrm{FT}^{-1}[\tilde{z}_1'\ z_2'\ z_3'\ z_4'\ z_5'\ z_6'\ z_7'\ z_8']_k^{\mathrm{T}},$$

$$z_k = [z_3'\ z_4'\ z_5'\ z_6']_k^{\mathrm{T}}. \tag{35}$$

Notes:

- A preconditioner can be constructed for any subregion by merely filling/overlaying with zeros that part of r_k which we do not wish to iterate. (e.g. if we only wished to iterate the components u_1 and u_2 in (5) then we would choose $r_k' = [0\ 0\ r_1\ r_2\ 0\ 0\ 0\ 0]^{\mathrm{T}}$ and proceed with steps (1–3) above.]
- We see that there is some "leaking" in that the values z_1', z_2', z_7' and z_8' are not all zero. However, there is enough information in the remaining z' components to provide a good preconditioner.

Enhanced Jacobi iteration

We now consider an enhancement of Jacobi iteration in which the update at any one point is made to anticipate the changes that will take place at neighbouring points in subsequent iteration steps. Consider the standard Jacobi iteration scheme for the linear version of (31) [i.e. $\sigma(u) = 0$] expressed in component form:

$$\delta u_{i,k} = u_{i,k+1} - u_{i,k} = A_{ii}^{-1}\left(f_i - \sum_{j=1}^{N} A_{ij} u_{j,k}\right)$$

$$= A_{ii}^{-1} r_{i,k}, \tag{36a}$$

where $u_{i,k}$ denotes the ith component of u at the kth iteration. The solution value $u_{i,k+2}$ at the next iteration step is then of the form:

$$u_{i,k+2} = u_{i,k+1} + A_{ii}^{-1}\left[f_i - \sum_{j=1}^{N} A_{ij}(u_{j,k} + \delta u_{j,k})\right]$$

$$= u_{i,k} + \delta u_{i,k} + A_{ii}^{-1}\left[r_{i,k} - \sum_{j=1}^{N} A_{ij}\,\delta u_{j,k}\right],$$

or

$$u_{i,k+2} = u_{i,k} + A_{ii}^{-1}\left(r_{i,k} - \sum_{\substack{j=1 \\ j \neq i}}^{N} \frac{A_{ij}}{A_{ii}} r_{j,k}\right). \tag{36b}$$

We have, therefore, expressed the solution after two Jacobi iterations in terms of the residuals of the first step.

Table 1

Jacobi algorithm									
N	16	32	64	128	256	512	1024	2048	4096
No. of iterations	52	108	222	457	940	1929	3957	8112	—
Time (sec) (spatial)	31	239	1902	1.5E4	—	—	—	—	—
Time (sec) (FFT)	4.7	13	46	177	736	3034	1.3E4	5.3E4	—
Enhanced Jacobi algorithm (2 neighbours)									
N	16	32	64	128	256	512	1024	2048	4096
No. of iterations	31	66	137	283	583	1198	2458	5037	—
Time (sec) (FFT)	3.6	10.3	33	125	513	2118	8725	3.6E4	—
Standard conjugate gradient algorithm									
N	16	32	64	128	256	512	1024	2048	4096
No. of iterations	5	9	15	22	32	47	68	98	141
Time (sec) (FFT)	2.0	2.6	6.5	16.8	49.4	145	418	1227	3650
Spectrally preconditioned conjugate gradient algorithm									
N	16	32	64	128	256	512	1024	2048	4096
No. of iterations	4	4	5	5	5	6	6	6	6
Time (sec) (FFT)	1.1	1.5	2.5	4.3	8.4	19.1	38.5	77.0	158

Equation (36b) itself does not provide any saving in computational effort. However, since the matrix elements A_{ij} decay rapidly away from the diagonal it is possible to arrive at a close approximation to $u_{i,k+2}$ by restricting the sum in (36b) to only near-neighbour influences. The approximate scheme then becomes:

$$u_{i,k+2} \approx u_{i,k} + A_{ii}^{-1}\left(r_{i,k} - \sum_{j \in \mathcal{N}} \frac{A_{ij}}{A_{ii}} r_{j,k}\right), \qquad (36c)$$

where $\mathcal{N}$ is the set of indices of the near-neighbours.

We note that the enhanced Jacobi scheme (36c) is of the same form as that in (36a) but the residual $r_{i,k}$ at point i has been adjusted by a weighted average of the residuals of its neighbours. Since the summation in (36c) only involves the near-neighbours there is virtually no additional cost involved. Apart from obtaining roughly "two iterations for the price of one" for this linear problem, the enhanced Jacobi scheme (36c) is particularly useful in a non-linear environment. For the fully non-linear problem (31), the standard Jacobi method has the property that neighbouring elements can interact strongly with one another causing overdamped behaviour in some situations and underdamped behaviour in others. By using the neighbour-weighted residuals the iteration scheme anticipates this strong neighbour interaction and inhibits the undesirable situation in which there is simultaneous failure of rock in a number of adjacent elements.

Numerical results

We compare the performance of the algorithms described in the previous two subsections with that of the standard Jacobi algorithm. Since the extension of these novel algorithms to non-linear problems is still under investigation, we restrict this comparison to a linear crack model [i.e. $\sigma(u) = 0$ in (31)]. One of the primary motivations for the use of the FFT was to improve the speed of calculation of the expensive of convolution products that are required when modelling extensive regions of plastic strain by the BE technique. We therefore also consider a non-linear crack model [i.e. $\sigma(u) \neq 0$ in (31)] and demonstrate the improvement in performance achieved by using the FFT over a spatially implemented algorithm. All the run times quoted in this section were obtained using a Macintosh IIcx computer.

A linear crack problem. In Table 1 run times and iteration performances of Jacobi, enhanced Jacobi, standard CG and PCG are compared for a problem with a single crack. The parameters for the crack are: $l = 256$, $p = 60$ MPa, $E = 70{,}000$ MPa and $\nu = 0.2$ while the stopping criterion used for all the runs was that the L_2-norm of the residual stress was less than 10^{-3} MPa (i.e. $\|r_2\|_2 \leqslant 10^{-3}$). The parameter N refers to the number of degrees of freedom for the crack problem. In Fig. 9 we plot $\log_2(T)$ vs $\log_2(N)$ where T is the run time quoted in Table 1. In order to determine a measure of the asymptotic (i.e. large N) performance of each of

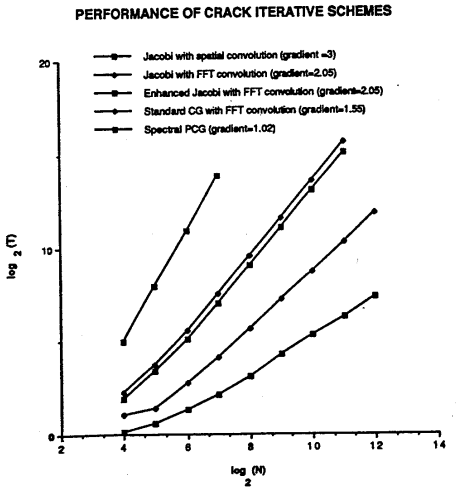

Fig. 9. A log–log plot of the execution time T vs the number N of degrees of freedom for the crack problem of Table 1. The asymptotic performance of the Jacobi, enhanced Jacobi, standard conjugate gradient and the preconditioned conjugate gradient algorithms can be seen from the gradients of the graphs.

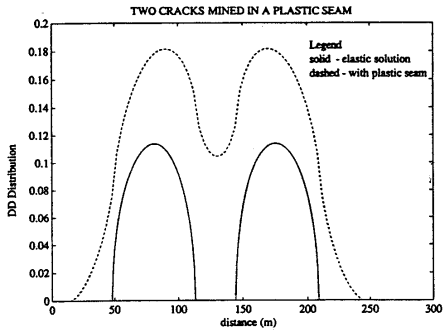

Fig. 10. The DD distribution for two crack-like excavations mined in a plastic seam which is embedded in an elastic medium. For the purposes of comparison, the elastic DD distribution is also plotted for two similar cracks that are mined in a homogeneous elastic body subjected to the same level of virgin stress.

the algorithms, the gradients quoted in this figure refer to the gradient of the line fitted to the last three points of each graph. We observe that the number of operations for the Jacobi algorithm using spatial convolutions grows as $O(N^3)$ while this is reduced to $O(N^2 \log N)$ if the FFT is used to perform the convolutions. The enhanced Jacobi method with only weighting from the two nearest neighbours is also an $O(N^2 \log N)$ algorithm but with a somewhat improved operation constant. We notice from Table 1 that the enhanced Jacobi method roughly halves the number of iterations required by the standard Jacobi method, but this improvement is not realized in the run times because of the additional computational burden of calculating the weighted residuals. The standard conjugate gradient algorithm using FFT convolutions reduces the operation count to roughly $O(N^{3/2} \log N)$. From Fig. 9 we see that the asymptotic performance of the spectral PCG algorithm is $O(N \log N)$—the number of operations it takes to perform a single iteration using the FFT. This is confirmed by the almost constant number of PCG iterations seen in Table 1.

A non-linear crack model. We consider two crack-like excavations each have a span of $2l = 64$ m and separated by a distance of 32 m to be mined in a perfectly plastic seam which is embedded in an otherwise elastic medium. Other run parameters are as follows: the virgin stress level is $p = 60$ MPa; the elastic constants are $E = 70{,}000$ MPa and $\nu = 0.2$; the yield strength of the plastic seam is $Y = 100$ MPa. The stopping criterion used for all the runs was that $\|r\|_2 = \|f - Au + \sigma(u)\|_2 \leq 10^{-3}$). The standard Jacobi algorithm was used to solve the equations as outlined in Fig. 5. In Fig. 10 the DD distribution for the two-crack plastic model is compared with the solution to the elastic two-crack model (i.e. without the plastic seam). As is to be expected the presence of the plastic seam increases DD components of the cracks. In Table 2 the required number of Jacobi iterations are given and the run time performances of the spatial and FFT convolution algorithms are compared. As was the case with the linear crack model, the spatial convolution algorithm requires $O(N^3)$ operations while the FFT convolution procedures reduces the number of operations to $O(N^2 \log N)$.

CONCLUSIONS

We have introduced a novel spectral method based on the FFT for solving boundary integral equations incorporating the effect of non-linear material behaviour. This new method can be used for direct and indirect BE formulations in both 2- and 3-D. Indeed the spectral BE technique can be implemented relatively easily in existing BE codes designed to model regular geometries such as planar excavations in 3-D. The computational advantages offered by the spectral BE approach could make the BE method a viable competitor to finite difference and finite element methods for modelling extensive regions of volumetric damage.

We have discussed the mathematical properties of this method which we have illustrated by means of a simple model problem. We have demonstrated that the spectral boundary element technique provides a whole new framework for volumetric modelling with easy access to a number of interesting features not available to spatially implemented algorithms. These new features include:

1. Efficient evaluation of convolution products in $O(N \log N)$ operations compared to the $O(N^2)$ operations required by algorithm based on direct spatial convolution. This feature not only accelerates solution times but can also be used to evaluate benchmark stresses and displacments in $O(N \log N)$ operations.
2. A fundamental set of point Fourier kernels from which a variety of approximation schemes (including the standard piecewise polynomial approximations) can be constructed in the frequency domain by introducing high-frequency filters. The frequency domain implementation of these approximation schemes avoids the tedious integrations associated with spatial discretizations of the integral equations and provides considerable flexibility for general purpose user-defined approximation schemes.
3. The FFT can be exploited to model periodically repeating mining geometries—such as those which occur in rib-pillar mining situations. We have also considered techniques that can be used to over-

Table 2. Performance of Jacobi scheme for two-crack plastic seam model

N	16	32	64	128
No. of iterations	65	126	246	471
Time (sec) spatial convolution	42	287	2127	15,993
Time (sec) FFT convolution	8.2	21.4	68	234

come the periodicity constraint imposed by the FFT so that general non-repeating geometries can be modelled.

4. Two novel iterative methods to solve the discretized BE equations efficiently. The first method uses the information provided by the FFT to construct an approximate inverse extremely efficient for use in a preconditioned conjugate gradient algorithm. This method [combined with the O(N log N) speed of the FFT for evaluating convolution products] can reduce the operation count for solution of the discretized problem from $O(N^3)$ to $O(N \log N)$ operations. One of the disadvantages of the spectrally preconditioned conjugate gradient method is that it requires three times more memory than that required by the standard Jacobi scheme. For large problems (particularly in 3-D) the additional memory that would be required could severely limit the number of degrees of freedom in the model. We therefore also considered a simple enhancement of the Jacobi iteration technique which does not require any additional memory and requires only a little extra computational effort. The enhanced Jacobi iteration can roughly double the convergence rate for linear problems and inhibits undesirable simultaneous failure of neighbouring elements when modelling brittle rock fracture.

Our objective in this paper has been to present the spectral boundary element algorithm and explore some of its properties. Rather than being exhaustive, this paper opens up a number of avenues of further research including: a rigorous error analysis of the various approximations introduced by filtering; the accuracy of the higher order filters when modelling non-linear material behaviour over large volumes of rock; the performance and robustness of the spectrally preconditioned conjugate gradient algorithm for a variety of non-linear material models; the extension of the spectral boundary element method to include irregular geometries; and an assessment of the relative accuracy and efficiency when compared with existing algorithms such as the finite difference and finite element methods.

Acknowledgements—The authors wish to acknowledge the support of the Chamber of Mines of South Africa and the National Science and Engineering Research Council of Canada. The authors are also grateful to Dr J. A. Ryder for useful discussions on the properties of the point Fourier kernels. The authors wish to thank the reviewers for their meticulous review of the manuscript.

Accepted for publication 31 January 1992.

REFERENCES

1. Spottiswoode S. Towards 3D modelling of inelastic deformation around deep-level mines. In *Mechanics of Jointed and Faulted Rock, Proc. Int. Conf., Vienna* (H. P. Rossmanith, Ed.). Balkema, Rotterdam (1990).
2. Crouch S. L. Analysis of stesses and displacements around underground excavations: an application of the displacement discontinuity method. Geomechanics Report to the National Science Foundation, University of Minnesota, MN (1976).
3. Cundall P. and Board M. A microcomputer program for modelling large-strain plasticity problems. In *Numerical Methods in Geomechanics (Innsbruck 1988)*, (Swoboda, Ed.). Balkema, Rotterdam (1988).
4. Banerjee P. K. and Cathie D. N. A direct formulation and implementation of the boundary element method for two-dimensional problems of elasto-plasticity. *Int. J. Mech. Sci.* **22**, 233–245 (1980).
5. Peirce A. P. The applicability of the nonlinear boundary element method in the modelling of mining excavations. M.Sc. Thesis, University of the Witwatersrand, South Africa (1983).
6. Gottlieb D. and Orszag S. A. *Numerical Analysis of Spectral Methods: Theory and Applications*. SIAM, Philadelphia (1977).
7. Canuto C., Hussaini M. Y., Quarteroni A. and Zang, *Spectral Methods in Fluid Dynamics, Springer Series in Computational Physics*. Springer-Verlag, New York (1987).
8. Banerjee P. K. and Butterfield, R., *Boundary Element Methods in Engineering Science*. McGraw-Hill, Maidenhead (1981).
9. Plewman R. P., Deist F. H. and Ortlepp W. D. The development and application of a digital computer method for the solution of strata control problems. *J.S. Afr. Inst. Min. Metall.* **70**, 214 (1969).
10. Press W. H., Flannery B. P., Teukolsky S. A. and Vetterling W. T., *Numerical Recipes*. Cambridge University Press (1986).
11. Stewart A. An application of the fast Fourier transform in numerical elasticity. M.Sc. Thesis, University of the Witwatersrand, South Africa (1979).
12. Vichnevetsky R. and Bowles J. B. *Fourier Analysis of Numerical Approximations of Hyperbolic Equations*. SIAM, Philadelphia (1982).
13. Ryder J. A. Rational function analysis of tabular excavations in two dimensions. Research Report No. 40/84, Chamber of Mines of South Africa Research Organization (1984).
14. Beale J. and Majda A. High order accurate vortex methods with explicit velocity kernels. *J. Comput. Phys.* **58**, 188–208 (1985).
15. Salamon M. D. G. Rock mechanics of underground excavations. *Proc. 3rd Congr. ISRM*, Denver, Vol. 2, pp. 951–1099 (1974).
16. Ryder J. A. and Ozbay M. U. A methodology for designing pillar layouts for shallow mining. In *Static and Dynamic Considerations in Rock Engineering, Proc. ISRM Conf., Swaziland* (R. Brummer, Ed.). B. Alkena, Rotterdam (1990).
17. Gradshteyn I. S. and I. M. Ryzhik, *Table of Integrals, Series and Products*. Academic Press, Orlando FL (1980).
18. Axelsson O. and Lindskog G. On the eigenvalue distribution of a class of preconditioning methods. *Numer. Math.* **48**, 478–498 (1986).
19. Axelsson O. and Lindskog G. On the rate of convergence of the preconditioned conjugate gradient method. *Numer. Math.* **48**, 499–523 (1986).
20. Chan R. H. and Strang G. Toeplitz equations by conjugate gradients with circulant preconditioner. *SIAM J. Sci. Statist Comput.* **10**, 104–119 (1989).
21. Jaswon M. A. and Symm G. T. *Integral Equation Methods in Potential Theory and Elastostatics*. Academic Press, London (1977).
22. Shilov G. E. *Generalized Functions and Partial Differential Equations*, p. 157. Gordon & Breach, NY (1968).

APPENDIX A

Potential Representations of the BE kernels

From equations (1a) and (1b) it can be seen that four fundamental influence kernels operate on the stress and displacement discontinuity densities to yield expressions for the displacements and stresses at any point in the medium. Equation (1a) is derived by considering a point force with components $e_k(p)$ to operate at point p in a region B bounded by the surface ∂B as shown in Fig. 1.

The inward normal to the surface at point q has components $n_i(q)$. The displacement vector arising at point q due to the point force applied at point p is given by Kelvin's solution for an isotropic elastic medium which can be represented in the form:

$$u'_i(q) = g(q_i, p_k)e_k(p), \tag{A1}$$

where summation over repeated subscripts is assumed. The stress components at point q are given by Hooke's Law:

$$\sigma'_{ij}(q) = \frac{E}{2(1+\nu)}\left[\frac{2\nu}{1-2\nu}\delta_{ij}u'_{m,m} + u'_{i,j} + u'_{j,i}\right].$$

Here commas are used to denote derivatives with respect to the coordinate components q_i. The stress components at q due to the point force at p can be written symbolically as:

$$\sigma'_{ij}(q) = G(q_{ij}, p_k)e_k(p). \tag{A2}$$

In (A1) and (A2) the vector and tensor indices are associated explicitly with the points q and p, following the notation convention adopted by Jaswon and Symm [21]. Now postulate two equilibrated displacement and stress fields u_i, σ_{ij} and $\bar{u}_i$, $\bar{\sigma}_{ij}$ associated, respectively, with the inner and outer regions B and $\bar{B}$ depicted in Fig. 1. By applying Betti's reciprocal theorem to the displacement and traction components u'_i, $\sigma'_{ij}n_j$ coupled in turn to each postulated field, it is possible to formulate two independent integral relations. Taking the difference between these two relations yields equation (1a) for the displacement at point p in terms of the jumps in the traction vector and displacement vector across surface ∂B at all points q of this surface. The tractions and displacement jumps are defined to be:

Traction discontinuity:

$$T_i(q) = [\bar{\sigma}_{ij}(q) - \sigma_{ij}(q)]n_j(q). \tag{A3}$$

Displacement discontinuity:

$$D_i(q) = \bar{u}_i(q) - u_i(q). \tag{A4}$$

The influence functions $\gamma(q_i, p_{kl})$ and $\Gamma(q_{ij}, p_{kl})$ in (1b) are derived by substituting (1a) into Hooke's Law. It can be seen that once the fundamental solution (A1) is known, all the influence functions $G(q_{ij}, p_k)$, $\gamma(q_i, p_{kl})$ and $\Gamma(q_{ij}, p_{kl})$ can be deduced by appropriate derivative operations at points q and p. Hence, defining the distance r between points q and p by:

$$r^2 = (q_i - p_i)(q_i - p_i) \tag{A5}$$

and noting that $\partial r/\partial q_i = (q_i - p_i)/r$, it is possible to write explicit relations for the influence functions in the following forms:

$$g(q_i, p_k) = \frac{(1+\nu)}{8\pi E(1-\nu)r}\left[(3-4\nu)\delta_{ik} + \frac{\partial r}{\partial q_i}\frac{\partial r}{\partial q_k}\right], \tag{A6}$$

$$G(q_{ij}, p_k) = \frac{1}{8\pi(1-\nu)r^2}\left[(1-2\nu)\left(\delta_{ij}\frac{\partial r}{\partial q_k} - \delta_{ik}\frac{\partial r}{\partial q_j} - \delta_{jk}\frac{\partial r}{\partial q_i}\right) - 3\frac{\partial r}{\partial q_i}\frac{\partial r}{\partial q_j}\frac{\partial r}{\partial q_k}\right], \tag{A7}$$

$$\gamma(q_i, p_{kl}) = \frac{1}{8\pi(1-\nu)r^2}\left[(1-2\nu)\left(-\delta_{kl}\frac{\partial r}{\partial q_i} + \delta_{ik}\frac{\partial r}{\partial q_l} + \delta_{il}\frac{\partial r}{\partial q_k}\right) + 3\frac{\partial r}{\partial q_i}\frac{\partial r}{\partial q_k}\frac{\partial r}{\partial q_l}\right], \tag{A8}$$

$$\Gamma(q_{ij}, p_{kl}) = \frac{E}{8\pi(1-\nu^2)r^3}\left[-(1-4\nu)\delta_{ij}\delta_{kl} + (1-2\nu)(\delta_{ik}\delta_{jl} + \delta_{jk}\delta_{il}) + 3(1-2\nu)\times\left(\delta_{kl}\frac{\partial r}{\partial q_i}\frac{\partial r}{\partial q_j} + \delta_{ij}\frac{\partial r}{\partial q_k}\frac{\partial r}{\partial q_l}\right) + 3\nu\times\left(\delta_{ik}\frac{\partial r}{\partial q_j}\frac{\partial r}{\partial q_l} + \delta_{il}\frac{\partial r}{\partial q_j}\frac{\partial r}{\partial q_k} + \delta_{jk}\frac{\partial r}{\partial q_i}\frac{\partial r}{\partial q_l} + \delta_{jl}\frac{\partial r}{\partial q_i}\frac{\partial r}{\partial q_k}\right) - 15\frac{\partial r}{\partial q_i}\frac{\partial r}{\partial q_j}\frac{\partial r}{\partial q_k}\frac{\partial r}{\partial q_l}\right]. \tag{A9}$$

In numerical applications in which the boundary surface ∂B is divided into "elements" and the influence functions are evaluated with specific shape functions applied to the traction and displacement discontinuity densities, it is convenient to express equations (A6)–(A9) in alternative forms. These can be expressed succinctly in terms of the derivatives of a biharmonic function Ψ and a harmonic function Φ and are particularly appropriate for the derivations of the transformed kernels discussed in the present paper. Also by a suitable choice of Ψ and Φ the kernels can be expressed in the same form in 3-D as well as 2-D plane strain.

In particular, the fundamental solution to the biharmonic equation $\nabla^4\Psi = 0$ is given by:

$$\Psi = r. \tag{A10}$$

By successively differentiating this function with respect to the coordinate components q_i, it can be shown that:

$$\Psi_{,i} = \frac{\partial r}{\partial q_i} = \frac{(q_i - p_i)}{r}, \tag{A11}$$

$$\Psi_{,ij} = \left(\delta_{ij} - \frac{\partial r}{\partial q_i}\frac{\partial r}{\partial q_j}\right)\Big/ r, \tag{A12}$$

$$\Psi_{,ijk} = \left(-\delta_{ij}\frac{\partial r}{\partial q_k} - \delta_{jk}\frac{\partial r}{\partial q_i} - \delta_{ik}\frac{\partial r}{\partial q_j} + 3\frac{\partial r}{\partial q_i}\frac{\partial r}{\partial q_j}\frac{\partial r}{\partial q_k}\right)\Big/ r^2, \tag{A13}$$

$$\Psi_{,ijkl} = \left[3\left(\delta_{ij}\frac{\partial r}{\partial q_k}\frac{\partial r}{\partial q_l} + \delta_{jk}\frac{\partial r}{\partial q_i}\frac{\partial r}{\partial q_l} + \delta_{ik}\frac{\partial r}{\partial q_j}\frac{\partial r}{\partial q_l} + \delta_{il}\frac{\partial r}{\partial q_j}\frac{\partial r}{\partial q_k} + \delta_{jl}\frac{\partial r}{\partial q_i}\frac{\partial r}{\partial q_k} + \delta_{kl}\frac{\partial r}{\partial q_i}\frac{\partial r}{\partial q_j}\right) - \delta_{ij}\delta_{kl} - \delta_{jk}\delta_{il} - \delta_{ik}\delta_{jl} - 15\frac{\partial r}{\partial q_i}\frac{\partial r}{\partial q_j}\frac{\partial r}{\partial q_k}\frac{\partial r}{\partial q_l}\right]\Big/ r^3. \tag{A14}$$

Similarly, the fundamental solution of Laplace's equation is the harmonic potential:

$$\Phi = \frac{1}{r} = \tfrac{1}{2}\Psi_{,ii} \tag{A15}$$

Taking derivatives of Φ with respect to the coordinate components at point q, it can be shown that:

$$\Phi_{,i} = \frac{\partial}{\partial q_i}\left(\frac{1}{r}\right) = -\left(\frac{\partial r}{\partial q_i}\right)\Big/ r^2, \tag{A16}$$

$$\Phi_{,ij} = \left(3\frac{\partial r}{\partial q_i}\frac{\partial r}{\partial q_j} - \delta_{ij}\right)\Big/ r^3. \tag{A17}$$

Substituting equations (A11–A14), (A16) and (A17) into expressions (A6–A9) for the influence kernels, it is possible to replace all derivatives of r with respect to the components q_i by terms containing the harmonic and biharmonic functions Φ and Ψ and their derivatives with respect to q_i. Specifically,

$$g(q_i, p_k) = \frac{1+\nu}{8\pi E(1-\nu)}[4(1-\nu)\Phi\delta_{ik} - \Psi_{,ik}], \tag{A18}$$

$$G(q_{ij}, p_k) = \frac{1}{8\pi(1-\nu)}[-\Psi_{,ijk} + 2\nu\delta_{ij}\Phi_{,k} + 2(1-\nu)(\delta_{jk}\Phi_{,i} + \delta_{ik}\Phi_{,j})], \tag{A19}$$

$$\gamma(q_i, p_{kl}) = \frac{1}{8\pi(1-\nu)}[\Psi_{,ikl} - 2\nu\delta_{kl}\Phi_{,i} - 2(1-\nu)(\delta_{ik}\Phi_{,l} + \delta_{il}\Phi_{,k})], \tag{A20}$$

$$\Gamma(q_{ij}, p_{kl}) = \frac{E}{8\pi(1-\nu^2)}[\Psi_{,ijkl} - 2\nu(\delta_{kl}\Phi_{,ij} + \delta_{ij}\Phi_{,kl}) - (1-\nu)(\delta_{ik}\Phi_{,jl} + \delta_{il}\Phi_{,jk} + \delta_{jk}\Phi_{,il} + \delta_{jl}\Phi_{,ik})]. \tag{A21}$$

Two-dimensional plane strain potential functions

It is possible to use equation (A15) to write these expressions in terms of fourth-order derivatives of Ψ only. However, it can also be shown that the form of equations (A18–A21) can be retained in the special case of plane strain elasticity if the following 2-D potential functions are used:

$$\Psi = \tfrac{1}{2}(r^2 - r^2\log r^2), \tag{A22}$$

$$\Phi = -\log r^2. \tag{A23}$$

In this case r is the distance in two-dimensions between points p and q and all component indices range over 1 and 2. Particular derivatives of Ψ and Φ are:

$$\Psi_{,i} = -(q_i - p_i)\log r^2; \quad \Phi_{,i} = -\frac{2}{r}\frac{\partial r}{\partial q_i},$$

$$\Phi_{,ij} = -\delta_{ij}\log r^2 - 2\frac{(q_i - p_i)(q_j - p_j)}{r^2};$$

$$\Phi_{,ij} = -\frac{2\delta_{ij}}{r} + \frac{4}{r^2}\frac{\partial r}{\partial q_i}\frac{\partial r}{\partial q_j} \tag{A24}$$

In particular, it should be noted that $\Psi_{,ii} = 2\Phi - 2$ in contrast to equation (A15). The 2-D plane strain line force solution corresponding to Kelvin's solution is:

$$g(q_i, p_k) = \frac{1+\nu}{4\pi E(1-\nu)}\left[(3-4\nu)\delta_{ik}\log\left(\frac{1}{r}\right) + \frac{\partial r}{\partial q_i}\frac{\partial r}{\partial q_k}\right] \tag{A25}$$

and the equivalence to equations (A18–A21) may be confirmed by substituting appropriate derivatives of the form (A24) into equation (A25) and repeatedly applying Hooke's law to the components of points q and p.

APPENDIX B

Fourier Transforms of the BE Kernels

Since the FTs of the 2-D kernels can be obtained from the FTs of the 3-D kernels by setting $\omega_3 = 0$ we only present the FTs for the 3-D kernels.

Fourier transforms of the harmonic and biharmonic potentials

Making use of (3c) we obtain:

$$\hat{\Phi}(\omega) = \lim_{\epsilon\to 0+}\int_{R3}\exp[-\mathrm{i}(\omega\cdot\mathbf{r}) - \epsilon r]r^{-1}\,\mathrm{d}\mathbf{r}^3$$

$$= \lim_{\epsilon\to 0+}\int_0^\infty\int_0^{2\pi}\int_0^{\pi}\exp(-\mathrm{i}\rho r\cos\phi - \epsilon r)r\sin\phi\,\mathrm{d}r\,\mathrm{d}\theta\,\mathrm{d}\phi = \frac{4\pi}{\rho^2}$$

and similarly with the biharmonic potential:

$$\hat{\Psi}(\omega) = \lim_{\epsilon\to 0+}\int_{R3}\exp[-\mathrm{i}(\omega\cdot\mathbf{r}) - \epsilon r]r\,\mathrm{d}\mathbf{r}^3$$

$$= \lim_{\epsilon\to 0+}\int_0^\infty\int_0^{2\pi}\int_0^{\pi}\exp(-\mathrm{i}\rho r\cos\phi - \epsilon r)r^3\sin\phi\,\mathrm{d}r\,\mathrm{d}\theta\,\mathrm{d}\phi$$

$$= \frac{-8\pi}{\rho^4},$$

where $\mathbf{r} = (q_1 - p_1, q_2 - p_2, q_3 - p_3)$, $r = |\mathbf{r}|$ and $\rho = \sqrt{\omega_1^2 + \omega_2^2 + \omega_3^2}$. A more rigorous derivation of these results can also be achieved using the theory of tempered distributions (see for example Ref. [22]).

Fourier transforms of the fundamental kernels

We now make use of property (FT P1) of the FT to take the appropriate derivatives of these potential functions to obtain:

$$\hat{g}_{ik} = \frac{1+\nu}{E(1-\nu)\rho^4}[2(1-\nu)\rho^2\delta_{ik} - \omega_i\omega_k],$$

$$\hat{G}_{ijk} = \frac{\mathrm{i}}{(1-\nu)\rho^4}[-\omega_i\omega_j\omega_k + \nu\delta_{ij}\omega_k\rho^2 + (1-\nu)(\delta_{jk}\omega_i + \delta_{ik}\omega_j)\rho^2],$$

$$\hat{\gamma}_{ikl} = \frac{-\mathrm{i}}{(1-\nu)\rho^4}[-\omega_i\omega_k\omega_l + \nu\delta_{kl}\omega_i\rho^2 + (1-\nu)(\delta_{ik}\omega_l + \delta_{il}\omega_k)\rho^2],$$

$$\hat{\Gamma}_{ijkl} = \frac{E}{2(1-\nu^2)\rho^2}\left[-\frac{2\omega_i\omega_j\omega_k\omega_l}{\rho^2} + 2\nu(\delta_{kl}\omega_i\omega_j + \delta_{jl}\omega_k\omega_l)\right.$$
$$+ (1-\nu)(\delta_{ik}\omega_j\omega_l + \delta_{il}\omega_j\omega_k + \delta_{jk}\omega_i\omega_l + \delta_{jl}\omega_i\omega_k)$$
$$\left. - 2\nu\delta_{ij}\delta_{kl}\rho^2 - (1-\nu)(\delta_{ik}\delta_{jl} + \delta_{jk}\delta_{il})\rho^2\right],$$

where the constant term $-2\nu\delta_{ij}\delta_{kl} - (1-\nu)(\delta_{ik}\delta_{jl} + \delta_{jk}\delta_{il})$ has been added to ensure that the stresses self-equilibrate.